Tran-SET

Transportation Consortium of South-Central States

*Solving Emerging Transportation Resiliency, Sustainability, and Economic Challenges through the Use of Innovative Materials and Construction Methods: From Research to Implementation*

# Study On Hybrid Model Combining Super Learner And Physics-based Models For SHM In Bridges Using Low-cost BWIM

**Project No. 20STUTA26**

**Lead University: The University of Texas at Arlington**

**Final Report**

**August 2021**

**Disclaimer**

The contents of this report reflect the views of the authors, who are responsible for the facts and the accuracy of the information presented herein. This document is disseminated in the interest of information exchange. The report is funded, partially or entirely, by a grant from the U.S. Department of Transportation's University Transportation Centers Program. However, the U.S. Government assumes no liability for the contents or use thereof.

**Acknowledgements**

The authors acknowledge the Tran-SET for providing the financial support of this study. The authors also would like to thank Project Review Committee, Do Soo Moon , Austin Mckeon, and Trent Ballard for their support and direction of the project.

# TECHNICAL DOCUMENTATION PAGE

| 1. Project No. | 2. Government Accession No. | 3. Recipient's Catalog No. |
|---|---|---|
| 20STUTA26 | | |

| 4. Title and Subtitle | 5. Report Date |
|---|---|
| Study On Hybrid Model Combining Super Learner And Physics-based Models For SHM In Bridges Using Low-cost BWIM | Aug. 2021 |
| | **6. Performing Organization Code** |
| **7. Author(s)**<br>PI: Dr. Suyun Ham (ORCID: 0000-0001-6375-211X)<br>Co-PI: Shih-ho Chao<br>Co-PI: Kyoeng Rok Ryu<br>GRA: Yin Chao Yu<br>GRA: Dafnik Saril Kumar David | **8. Performing Organization Report No.** |
| **9. Performing Organization Name and Address**<br>Transportation Consortium of South-Central States (Tran-SET)<br>University Transportation Center for Region 6<br>3319 Patrick F. Taylor Hall, Louisiana State University, Baton Rouge, LA 70803 | **10. Work Unit No. (TRAIS)** |
| | **11. Contract or Grant No.** |
| **12. Sponsoring Agency Name and Address**<br>United States of America<br>Department of Transportation<br>Research and Innovative Technology Administration | **13. Type of Report and Period Covered**<br>Final Research Report<br>Aug. 2020 – Aug. 2021 |
| | **14. Sponsoring Agency Code** |

**15. Supplementary Notes**

Report uploaded and accessible at Tran-SET's website (http://transet.lsu.edu/).


**16. Abstract**

The main objective of this project is to study and develop hybrid models of BWIM physics-based models incorporates with SHM inspection used by artificial intelligence (AI) techniques to predict structural damage.
This study presents a comprehensive assessment of FE simulations leveraging contact method verified by vehicle-bridge interaction(VBI) theory and uses machine learning (ML) techniques to identify and predict structural damages from the structural response automatically. Bridges are a fundamental part of infrastructure management. The main challenge that we face is the aging of these transportation infrastructures without a tool to perform accurate structural assessments in a real-time manner. Unfortunately, this topic is still not completely developed due to the lack of study upon BWIM simulations designed with several different severity damages. The Contact method, a new approach to simulating moving-vehicle motion in BWIM simulation, is to carry out actual structural response verified by the VBI with comprehensive parameter studies. In order to simulation the reality complex condition of the bridge, the FE model is designed by four different classes of damages with three different damage locations applied with two different load conditions (e.g., static load and moving load). The responses collected from FE simulation are used for structural damage prediction leveraging the ML damage prediction model. Among ML methods, the XGBoost with assembly decision tree shows the most reliable results. *The results* in this project indicate that structural damage prediction can be achieved by using the ML technique and BWIM structural response, which provides high accuracy of damage prediction.


| 17. Key Words | 18. Distribution Statement |
|---|---|
| BWIM, SHM, VBI, FE, damage prediction, contact method, moving load | No restrictions. This document is available through the National Technical Information Service, Springfield, VA 22161. |

| 19. Security Classif. (of this report) | 20. Security Classif. (of this page) | 21. No. of Pages | 22. Price |
|---|---|---|---|
| Unclassified | Unclassified | 63 | |

**Form DOT F 1700.7 (8-72)** **Reproduction of completed page authorized.**

# SI* (MODERN METRIC) CONVERSION FACTORS

## APPROXIMATE CONVERSIONS TO SI UNITS

| Symbol | When You Know | Multiply By | To Find | Symbol |
|---|---|---|---|---|
| | | **LENGTH** | | |
| in | inches | 25.4 | millimeters | mm |
| ft | feet | 0.305 | meters | m |
| yd | yards | 0.914 | meters | m |
| mi | miles | 1.61 | kilometers | km |
| | | **AREA** | | |
| $in^2$ | square inches | 645.2 | square millimeters | $mm^2$ |
| $ft^2$ | square feet | 0.093 | square meters | $m^2$ |
| $yd^2$ | square yard | 0.836 | square meters | $m^2$ |
| ac | acres | 0.405 | hectares | ha |
| $mi^2$ | square miles | 2.59 | square kilometers | $km^2$ |
| | | **VOLUME** | | |
| fl oz | fluid ounces | 29.57 | milliliters | mL |
| gal | gallons | 3.785 | liters | L |
| $ft^3$ | cubic feet | 0.028 | cubic meters | $m^3$ |
| $yd^3$ | cubic yards | 0.765 | cubic meters | $m^3$ |
| | | NOTE: volumes greater than 1000 L shall be shown in $m^3$ | | |
| | | **MASS** | | |
| oz | ounces | 28.35 | grams | g |
| lb | pounds | 0.454 | kilograms | kg |
| T | short tons (2000 lb) | 0.907 | megagrams (or "metric ton") | Mg (or "t") |
| | | **TEMPERATURE (exact degrees)** | | |
| °F | Fahrenheit | 5 (F-32)/9<br>or (F-32)/1.8 | Celsius | °C |
| | | **ILLUMINATION** | | |
| fc | foot-candles | 10.76 | lux | lx |
| fl | foot-Lamberts | 3.426 | $candela/m^2$ | $cd/m^2$ |
| | | **FORCE and PRESSURE or STRESS** | | |
| lbf | poundforce | 4.45 | newtons | N |
| $lbf/in^2$ | poundforce per square inch | 6.89 | kilopascals | kPa |

## APPROXIMATE CONVERSIONS FROM SI UNITS

| Symbol | When You Know | Multiply By | To Find | Symbol |
|---|---|---|---|---|
| | | **LENGTH** | | |
| mm | millimeters | 0.039 | inches | in |
| m | meters | 3.28 | feet | ft |
| m | meters | 1.09 | yards | yd |
| km | kilometers | 0.621 | miles | mi |
| | | **AREA** | | |
| $mm^2$ | square millimeters | 0.0016 | square inches | $in^2$ |
| m | square meters | 10.764 | square feet | $ft^2$ |
| m | square meters | 1.195 | square yards | $yd^2$ |
| ha | hectares | 2.47 | acres | ac |
| km | square kilometers | 0.386 | square miles | $mi^2$ |
| | | **VOLUME** | | |
| mL | milliliters | 0.034 | fluid ounces | fl oz |
| L | liters | 0.264 | gallons | gal |
| m | cubic meters | 35.314 | cubic feet | $ft^3$ |
| m | cubic meters | 1.307 | cubic yards | $yd^3$ |
| | | **MASS** | | |
| g | grams | 0.035 | ounces | oz |
| kg | kilograms | 2.202 | pounds | lb |
| Mg (or "t") | megagrams (or "metric ton") | 1.103 | short tons (2000 lb) | T |
| | | **TEMPERATURE (exact degrees)** | | |
| C | Celsius | 1.8C+32 | Fahrenheit | °F |
| | | **ILLUMINATION** | | |
| lx | lux | 0.0929 | foot-candles | fc |
| $cd/m^2$ | $candela/m^2$ | 0.2919 | foot-Lamberts | fl |
| | | **FORCE and PRESSURE or STRESS** | | |
| N | newtons | 0.225 | poundforce | lbf |
| kPa | kilopascals | 0.145 | poundforce per square inch | $lbf/in^2$ |

# TABLE OF CONTENTS

## LIST OF FIGURES

# LIST OF TABLES

## ACRONYMS, ABBREVIATIONS, AND SYMBOLS

| | |
|---|---|
| SHM | Structural health monitoring |
| DAQ | Data acquisition device |
| DANN | Deep artificial neural network |
| FE | Finite element |
| VBI | Vehicle-bridge interaction |
| BWIM | Bridge weight-in-motion |
| AI | Artificial intelligence |
| ML | Machine learning |
| ANN | Artificial neuron network |
| BP | Backpropagation |
| SVM | Support vector machine |
| DT | Decision tree |

## EXECUTIVE SUMMARY

Bridge-based weight-in-motion systems (BWIM) use the structure's response to estimate a vehicle's load distribution. BWIM can be a candidate that overcomes the critical challenges of structural health monitoring (SHM) in versatility across various bridge structure types and conditions. Although BWIM for SHM has been well-studied, there still exist technical challenges in the current BWIM system. In particular, to improve the accuracy of BWIM systems, it is imperative to adopt advanced methods that integrate identification and prediction in low-cost BWIM systems, such as machine learning (ML) models (e.g., artificial neural network and gradient boosting). Recently, ML models have been adopted for BWIM. However, it is often claimed that they do not accomplish sufficient prediction power for damage prediction. In response, we need more advanced ML and neural network systems.

A series procedure for damage prediction will be devised and applied based on a comparative assessment of physics-based FE model and ML models, including contact method, feature selection, and data prediction model. In general, ML requires a large database to train the prediction model. The input, known as the structural response, is one of the most important responses for the database collected from FE simulation. Thus, the comprehensive parameter study between FE simulation and vehicle-bridge interaction analytical solution is discussed to verify the correctness of FE simulation results. Furthermore, to avoid bad training situations or overfitting during the ML model training stage, the feature selection technique is used to extract the significant information from structural responses to improve the accuracy of damage prediction results. In addition, the damage prediction results using different ML models are compared.

The results indicate that among damage prediction models, the XGBoost shows the most reliable result with the highest prediction accuracy. Furthermore, the physics-based model applied with contact method leveraging AI techniques demonstrates a possibility for SHM by using BWIM response, which provides cost-effectiveness and reliable procedure of performing accurate structural assessments in a real-time manner.

# 1. INTRODUCTION

Bridges are a fundamental part of infrastructure management. The main challenge that we face is the aging of these transportation infrastructures without a tool for performing accurate structural assessments in a real-time manner. Thus, there is a need for a cost-effective and reliable assessment procedure. Many structural health monitoring (SHM) techniques have been devised over the past decades. However, there is no particular solution that can be applied to various bridges with different conditions. Bridge-based weight-in-motion systems (BWIM) use the structure's response to estimate a vehicle's load distribution addressing some of the shortcomings of traditional pavement weight-in-motion (WIM) systems [1]. This technology is primarily used to obtain vehicle axle weights without inconvenience and interruption to the traveling public and traffic. BWIM can be of use also in damage detection [2].

BWIM can be a candidate that overcomes the shortfall of SHM. Although BWIM for SHM has been well-studied [2]–[4], there still exist technical challenges in the current BWIM system due to many factors; inaccurate WIM system, inconsistent traveling speed, and limitations in the application to different types of bridge. For example, TRB report [5] states that there are gaps that exist in the current state of WIM practice, including the following: 1) despite considerable interest, BWIM capabilities are not being fully utilized or pursued in the United States, and 2) further initiatives are needed to advance BWIM successfully beyond research and limited applications.

Furthermore, the accuracy of BWIM systems needs to be improved by incorporating advanced technology. Machine-learning (ML) models (e.g., artificial neural network and gradient boosting) can be a solution to the integration of identification and prediction in BWIM systems. Gonzalez and Karoumi studied BWIM for SHM using the ML model [6], and their BWIM-aided damage detection method has two stages: 1) artificial neural network (ANN) and 2) Gaussian process. This two-stage model is likely to overfit the data, and its performance cannot be generalized to a population. Inputs of their method (deck acceleration) arrive sequentially over time and show spatial correlation because the inputs are measured by an array of sensors. However, their basic feed-forward ANN structure does not account for the Spatio-temporal correlation between sensor nodes to detect outlier data. Therefore, it causes a lack of prediction of damage detection.

To improve the prediction power of damage detection, we will carefully consider the Spatio-temporal correlation by ML models. The project's primary goal is to enhance BWIM systems for SHM simply by performing additional calculations of the measurements based on ML models, especially using deep artificial neural network (DANN) based BWIM (DN-BWIM).

## 2. OBJECTIVES

The main goal of this project is to study and develop hybrid models of physics-based models incorporates with SHM inspection used by artificial intelligence (AI) techniques to predict structural damage. Thus, there are several main objectives: 1) lab test and sensor configuration, 2) field test with different types of vehicle and different moving speed, 3) study and develop moving load FE model to simulate reality vehicle motion with contact method; 4) verify FE model and implement comprehensive parameter study by using vehicle-bridge interaction (VBI); and 5) apply several different ML models to compare which one brings more reliable with high-accuracy for damage prediction.

Based on these objectives, the team performed steven tasks: Task 1. literature review; Task 2. select local bridge location; Task 3. sensor configuration and sensor performance test; Task 4. field test; Task 5. In-depth study of finite element (FE) model simulation with static load and moving load; Task 6. development of machine learning model for damage prediction.

# 3. LITERATURE REVIEW

Bridges are a fundamental part of infrastructure management. The main challenge that we face is the aging of these transportation infrastructures without a tool for performing accurate structural assessments in a real-time manner. There is a need for a cost-effective and reliable assessment procedure. Many SHM techniques have been developed over the past decades. However, there is no particular solution that can be applied to diverse bridges with different conditions. BWIM uses the structure's response to estimate a vehicle's load distribution addressing some of the shortcomings of the traditional pavement WIM systems [1]. This technology is primarily used to obtain vehicle axle weights without inconvenience and interruption to the traveling public and traffic. BWIM can be a candidate that overcomes the shortfall of SHM. Although BWIM for SHM has been well-studied [2]–[4],

In recent years, there has been an increase in the development of structural health monitoring (SHM) techniques to assess and evaluate the safety of bridges [7]. [8] provide the approaches for pavement-based and bridge-based weight-in-motion (WIM). [9] summarized the advantages of SHM, for example, extending the service life of the bridge through a proper health assessment and appropriate maintenance activities. SHM of bridges helps in detecting specific problems in loading conditions that may lead to possible structural damages [10]. [11] discussed the value propositions for SHM supporting bridge management and the suitable frameworks to engage SHM in delivering bridge management value. The SHM process can provide real-time information to assess safety after disasters [10]. BWIM also can be of use in damage detection. [12] used virtual axle concept with Monte Carlo numerical method to detect damage. [4] used statistical analysis with acceleration for detecting damage. (Neves et al., 2018) designed FE modeling for collecting data of structural response to detect damage. Besides, technical challenges in the current BWIM system still exist due to many factors: inaccurate WIM system, inconsistent traveling speed, and limitations in the application to different types of bridges. For example, TRB report [5] states that there are gaps that exist in the current state of WIM practice, including the following: 1) despite considerable interest, BWIM capabilities are not being fully utilized or pursued in the United States, and 2) further initiatives are needed to advance BWIM successfully beyond research and limited applications.

Moreover, there are still some challenges of SHM. For example, it is impossible to predict damage before a disaster. The new trend within these three years of SHM is to focus on damage detection after the disaster and discover a method of predicting damage before the disaster. ML models (e.g., artificial neural network and gradient boosting) can be a solution to the integration of identification and prediction in BWIM systems. For damage prediction, large databases regarding structural response in different damage incorporated with AI technique are required. [14] achieved damage prediction with binary damage (e.g., crack and no crack) based on FE modeling and random forest model. (Neves et al., 2018) predicted two types of damages in flange and bracing with acceleration by using artificial neural network (ANN). [15] used ANN with structural data simulated from numerical equations to predict bridge damage. [16] used structural acceleration and Discrete Fourier Transform (DFT) spectrum of acceleration from numerical analysis with ANN to recognize damage. Civil engineers have started devoting time to developing bridge damage prediction with machine learning model these years. Unfortunately, this topic is still not completely developed. The severity of damage is not realistic since the actual damage is not just two or three types of damage, but could vary depending on the serving time and bearing capacity of bridge. Besides, there are few studies for comparing different types of machine learning

model for damage prediction, and it is valuable to find out which machine learning model gives more accuracy of damage predication. Moreover, there is not only a lack of comprehensive comparison between machine learning model for damage prediction but also a lack of damage prediction between static load and moving load. The flowchart of this report is shown in Figure 1. Stage 1 is regarding data collection from FE modeling, and stage 2 is an application of AI technique for damage prediction. In stage 1, the realistic structural responses are gained by using static and moving load. In stage 2, the feature selection is applied for extracting the important part of data collected from stage 1 as input for ML models. This process improves the accuracy of damage prediction.

**The main goal of this project** is to study and develop hybrid models of physics-based models incorporates with SHM inspection used by artificial intelligence (AI) techniques to predict structural damage. Thus, there are several main objectives: 1) Sensor configuration and field test, 2) configuration between field test and FE model simulation, 3) study and develop moving load FE model to simulate reality vehicle motion with contact method; 4) verify FE model and implement comprehensive parameter study by using vehicle-bridge interaction (VBI); and 5) apply several different ML models to compare which one brings more reliable with high-accuracy for damage prediction.

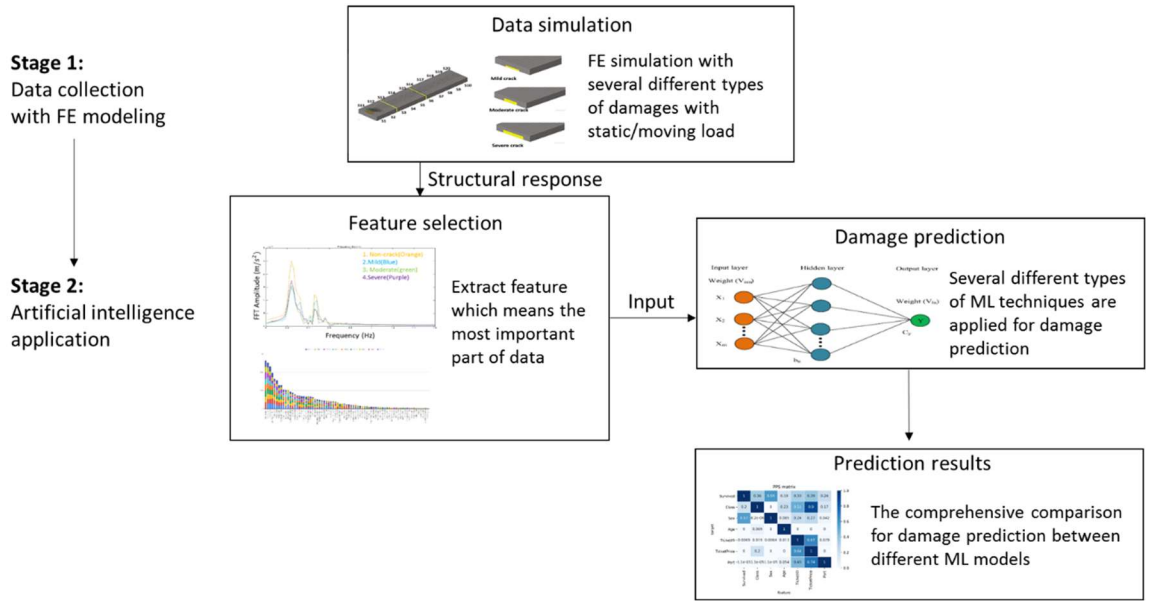


Figure 1. The flowchart of the paper. Stage 1 is regarding data collection from FE modeling, and stage 2 is an application of AI technique for damage prediction. In stage 1, the realistic structural responses are gained by using static and moving load. In stage 2, the feature selection is applied for extracting the important part of data collected from stage 1 as input for ML models. This process improves the accuracy of damage prediction.

# 4. METHODOLOGY

In this section, all tasks and their approaches will be delivered one by one. In Task 2, the research team provides and surveys four bridge candidates in the local area. In Task 3, the sensor calibration and two different scale lab test will be delivered. The field test preparation is described in Task 4. The in-depth physics-based finite element model study is in Task 5. The machine learning pre-processing and algorithm are in Task 6. All results are shown one by one in Chapter 5. For finding the relationship between gross vehicle weight (GVW) and displacement variation, the tendency curve and statistical box plot are shown. The comprehensive, in-depth FE model simulation parameter study with three different crack damages (e.g., mild crack, moderate crack, and severe crack) and load conditions (e.g., static load and moving load) are also shown in Chapter 5. The developed moving-load-based FE computation approach, kinetic contact enforcement method (or contact method) is further proved by vehicle bridge interaction equations. The last is AI technology used to predict structural damage, including feature selection and damage prediction models.

## 4.1 Task2: Select Local Bridges to Install BWIM:

We have four bridge candidates to select the appropriate bridge for a field test as shown in Figure **2**. Figure **3** presents the first candidate, Bridge 1) is located on S Mesquite St. in Arlington (32.724431,-97.104510). The bridge has a total 60m length and two different spans as 20m and 14m width. The second candidate, Bridge 2, is located on Center St. Trail Arlington (32.72439,-97.10490). The bridge has an overall length of 64 m and a width of16m, as shown in Figure **4**. The third candidate(Bridge 3) is located on W Mitchell St, Arlington (32.726921, -97.111945), as shown in Figure **5**. Figure **3**The bridge has an overall length of 20m. The fourth candidate(Bridge 4) is located in central Arlington (32.727727, -97.114594), as shown in Figure **6**. Figure **3**The bridge material has a total length is 20m.

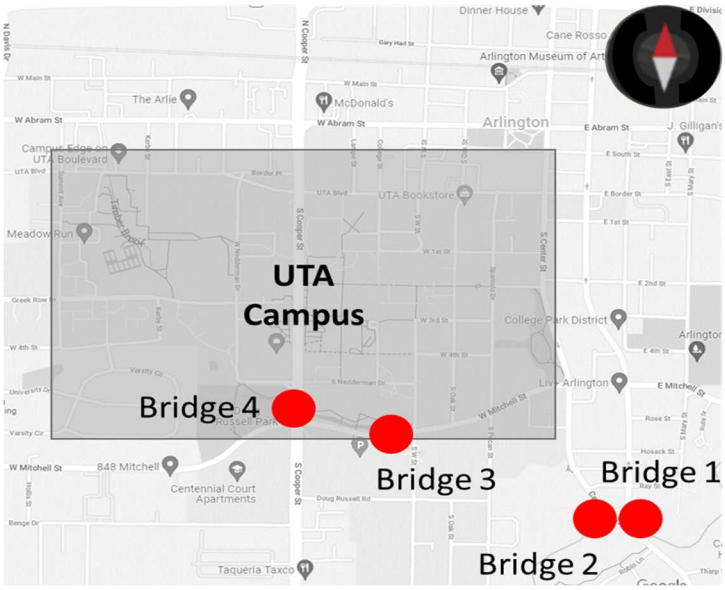


Figure 2. Overview of bridge candidate Location from a map


Figure 3. The photo of the first candidate (Bridge 1) on S Mesquite St. Arlington


Figure 4. The photo of the second candidate(Bridge 2) on Center St. Trail Arlington


Figure 5. The photo of the third candidate(Bridge 3) on W Mitchell St, Arlington.


Figure 6. The photo of the fourth candidate(Bridge 4) on Central Arlington.

To determine bridge for successful field tests, the preliminary test is performed considering the environmental issue such as traffic situation. The preliminary test is conducted with an accelerometer, as shown in Figure **7**, manufactured by PCB corporation (model number: 353B15) to collect acceleration during vehicle moving. The purpose of Task 2 is to choose an appropriate bridge for the future field test, while Task 3 laboratory tests include several sensor performance tests with detailed information of all testing equipment, including data acquisition (DAQ) and other types of sensors.

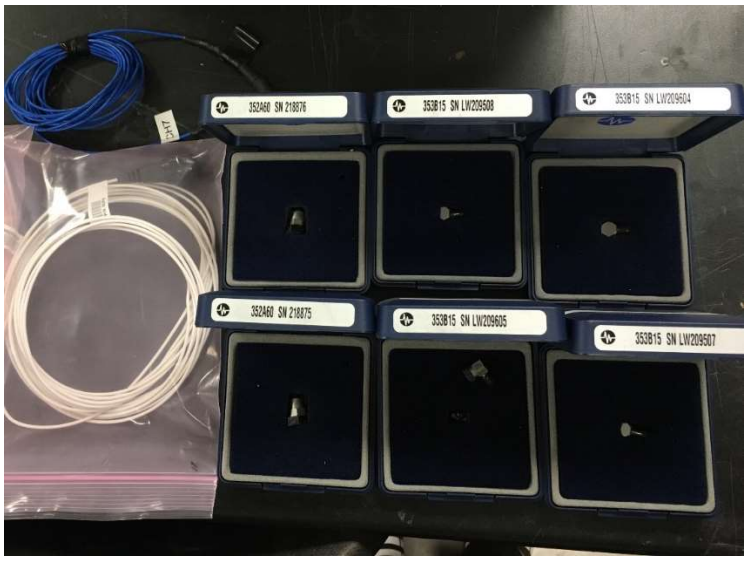


Figure 7. The accelerometer used for preliminary test in Task 2 to choose which bridge is the best field test location from candidates. The accelerometer made from PCB corporation (model number: 353B15). As a preliminary test, before selection of bridge, the team will do test in different bridges to make sure to get signal.

The summary of bridge information, including traffic situation and important environmental factors, are simply described in Table 1.

Table 1. The simple description of traffic condition and environment of each bridge candidate

| Bridge | Length | Material | Traffic condition | Environment issue (The difficulty of sensor deployment) |
|---|---|---|---|---|
| Bridge1 | 60(m) | Concrete pavement | Low(traffic mostly start from 5 pm) | Good |
| Bridge2 | 64(m) | Concrete pavement | Low(traffic mostly start from 5 pm) | Moderate, but hard to deploy sensor in the middle of the span |
| Bridge3 | 20(m) | Asphalt pavement | High | Bad(water) |
| Bridge4 | 20(m) | Concrete pavement | High | Bad(water) |

## 4.2 Task3: Preparation of Different Types of Sensors through a Laboratory Test

In this task, two laboratory tests are held in the civil engineering laboratory building(CELB) in UTA. The first laboratory test is a small-scale test to check the sensor's performance and calibration. The sensors are 1) accelerometer, 2) linear variable differential transformer (LVDT),

3) strain gauge, 4) low-cost linear potentiometer position sensor, and 5) low-cost draw-wire displacement linear sensor, as shown in Figure 8. The price and more information as shown in Table 2. To collect data from different sensors, we use two different DAQ and one amplifier. Strain gauge data and LVDT use Vishay Precision Group (VPG) DAQ to collect data, while the accelerometer and low-cost linear potentiometer position sensor use National Instrument (NI) DAQ. In addition, the team performs two different low-cost systems; and the other low-cost draw-wire displacement linear sensor use microcontroller to collect data. The type and information as shown in Figure 9 and Table 3. This first laboratory test aims to compare sensor performance, especially sensitivity. This dimension test specimen is 20-inch in length, 6-inch height and 6-inch width. Five different types of sensors are deployed under the middle of the concrete beam. The simulated moving load is applied with a wheel pushed by hand—the first laboratory test sensor deployment as shown in Figure 10.

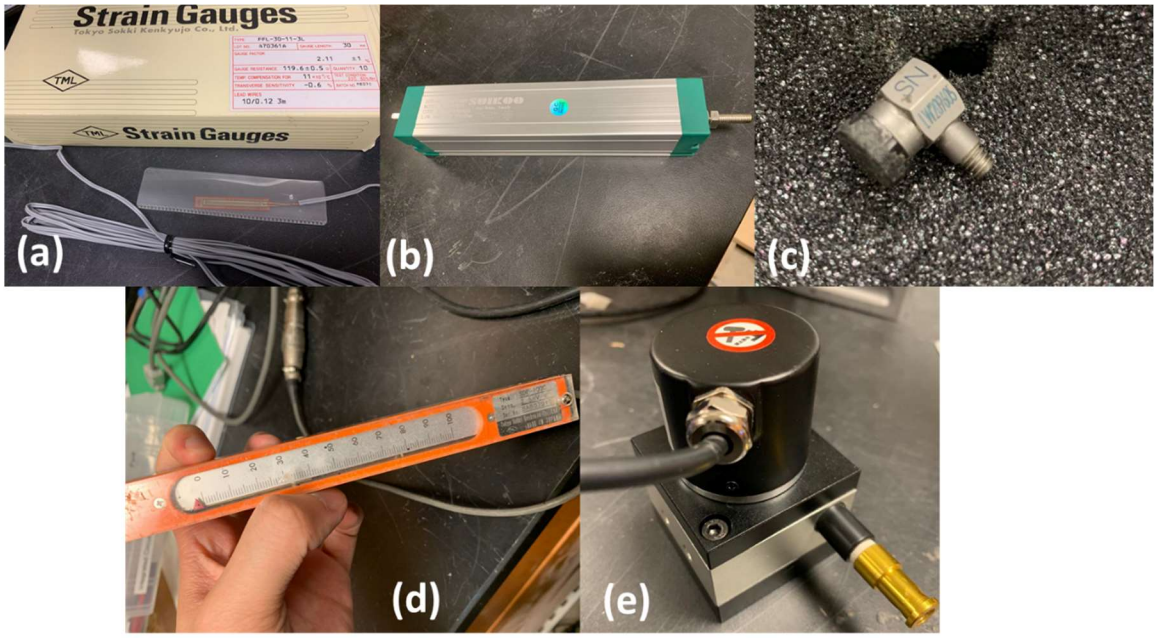


Figure 8. Different types of sensors used in laboratory test: (a) strain gauge, (b) linear potentiometer position sensor, (c) PCB accelerometer, (d) LVDT, and (e) draw-wire displacement linear sensor

Table 2. The information of five different sensors

| | **Strain gauge** | **Linear variable differential transformer( LVDT)** | **PCB accelerometer** | **Linear potentiometer position sensor** | **Draw-wire displacement linear sensor** |
|---|---|---|---|---|---|
| Company | Tokyo Sokki Kenkyujo Co.Ltd | Tokyo Sokki Kenkyujo Co.Ltd | PCB Piezotronics | Fafeicy | Calt |
| Model number | FFL-30-11-3L | SDP-1000 | 35B15 | KTC-100 | 5-24V-NPN |
| Resolution | 50000 ($10^6$ strain) | 0.01mm | 10 mV/g | Unlimited | 0.2 mm /pulse resolution |
| Price | $5 | $1000 | $300 | $30 | $76 |
| Data acquisition device (DAQ) used | VPG DAQ | NI DAQ | VPG DAQ | NI DAQ and amplifier | Micro-controller |


(a) NI DAQ (b) Signal amplifier


(c)VPG DAQ

Figure 9.The photo of data acquisition device(DAQ) (a) NI DAQ ,b) signal amplifier and(c) VPG DAQ

Table 3. The information of data acquisition device(DAQ) and signal amplifier

| | NI DAQ | PVG DAQ | Amplifier | Microcontroller |
|---|---|---|---|---|
| Company | National Instruments | Micro-Measurements | Kistler | Arduino |
| Model number | USB-6366 | Model 800-8-5n | 5134B | Mega2560 |
| Price | $5244 | $2000 | $895 | $40 |

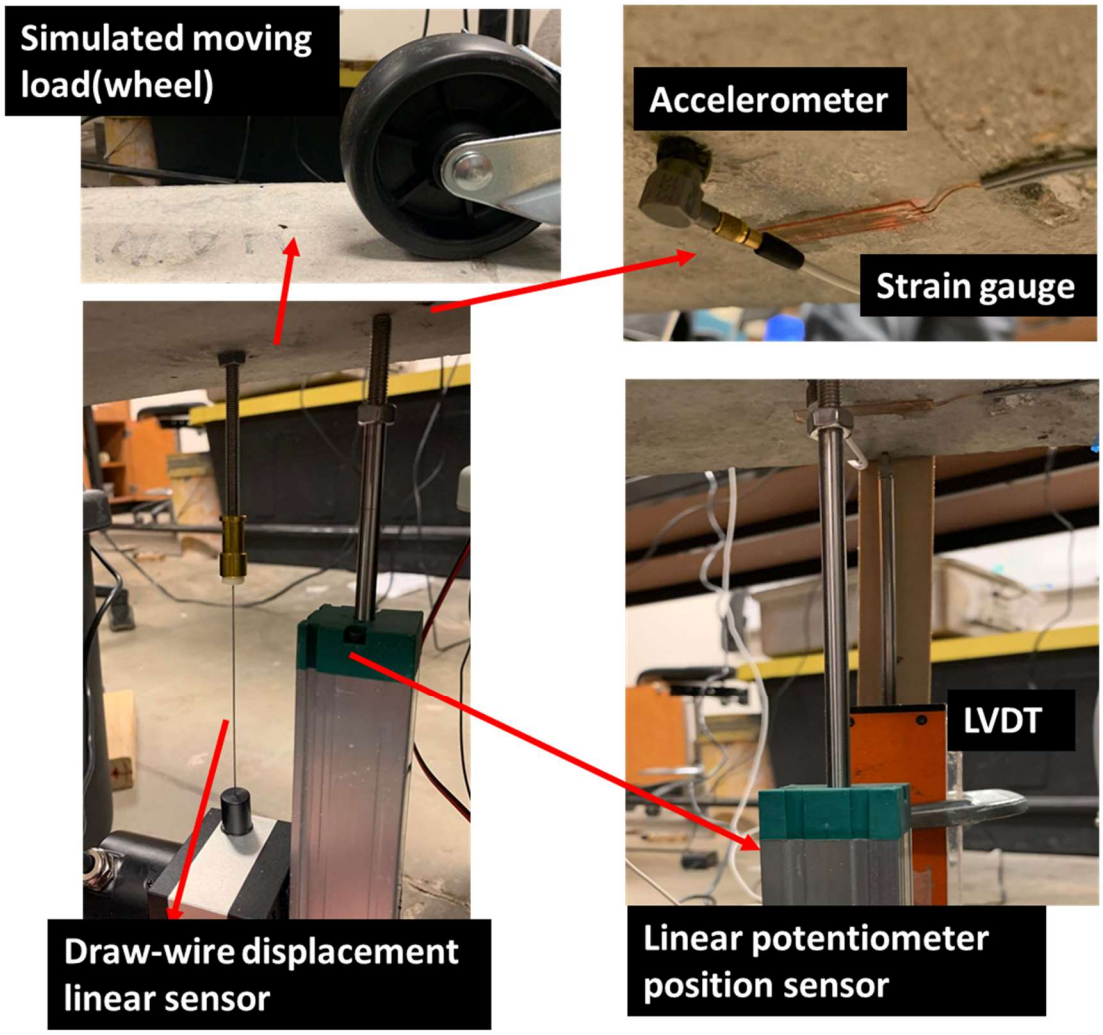


Figure 10. Testing configuration of the first laboratory test.

The second laboratory test is on a large-scaled beam structure deploying with LVDT and strain gauge, which are placed under the middle of the specimen. This test aims to obtain reference data for comparing the performance of different sensors in the field and make a good connection between experiment data and FE model simulation. Once the confirmation between experiment and simulation data is finish , ultimately FE model simulation can provide reliable data to machine learning(ML) work which are discussed in Task6.

The test specimen and testing configuration are as shown in Figure 11. The specimen dimension is 3m (118 in.) length, 0.4m (16 in.) width and 0.6m (24 in.) height. Five 0.5-inch diameter prestressing strands (ASTM A416, Grade 270, stress relieved) and a total of 16-#10 stirrups are used. Initial prestressing of 1201MPa (174 ksi) was applied to each strand, which in turn gave an average initial prestress of 2.48 MPa (359 psi) in the beams. The additional non-prestressed mild steel reinforcement (Grade 60) is used besides prestressing strands. The shear span to effective depth ratio was selected to be 3.0. Beams with this ratio belong to slender beams and usually give the lowest shear strength for beams without stirrups. A static load is added on the top middle

surface. The data mainly collected is the displacement and strain before the concrete beam goes to failure.

The single static load FE simulation model is shown in Figure 12. We also start to study and develop a finite element model in this task. The goal of this FE model is to use a laboratory test as a reference to develop a trustable physics-based FE model to create more valuable data. The detail and study for FE modeling both static load and moving load(moving vehicle) are described in section 4.4.

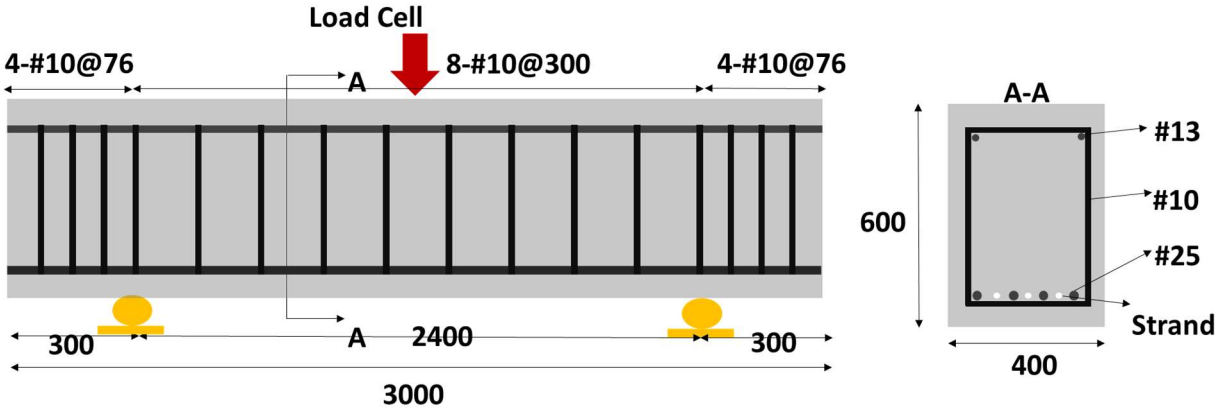


Figure 11. A testing configuration with concrete bean in the second laboratory test.

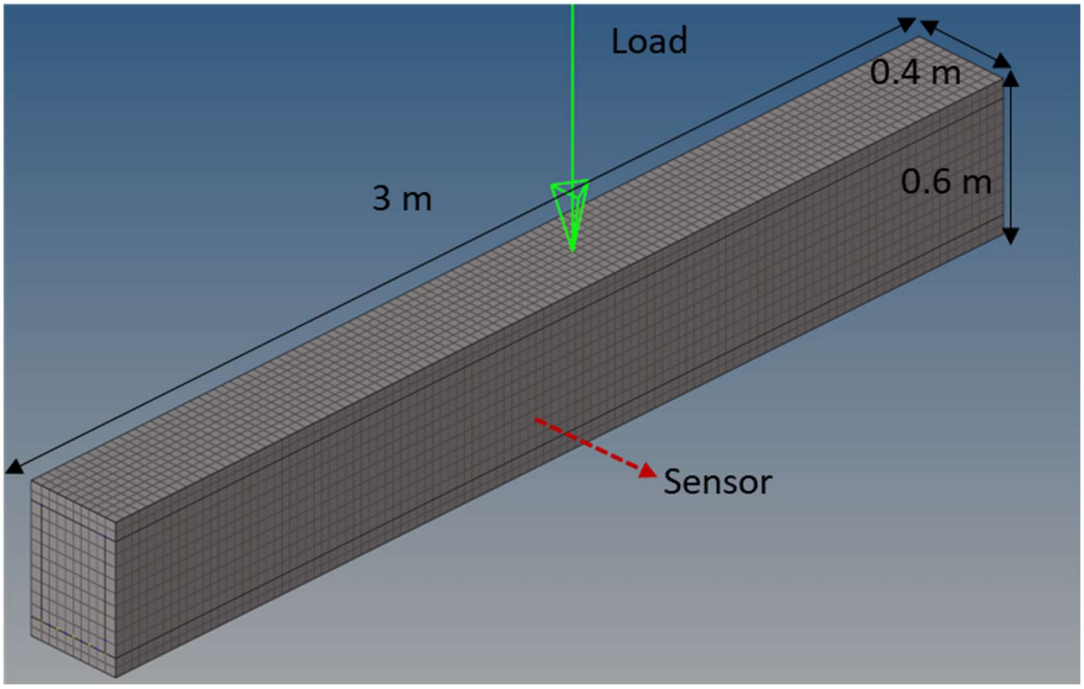


Figure 12. The Finite element model of laboratory test

## 4.3 Task4: Deployment of the BWIM

### *4.3.1 Field Test*

Task 4 includes field test information. The field test location is Bridge 1 (S Mesquite St. Arlington), proposed in Task2, which provides a good setup environment and low traffic situation for accurate and reliable tests. There is a retaining wall to hold the device, which means there is no requirement on the sensing wire length. Also, the research team can set strain gauge, accelerometer, LVDT, low-cost linear potentiometer position sensor, and low-cost draw-wire displacement linear sensor easily under the bridge deck. The bridge has seven girders with three one-way driving lanes. The sensors are deployed on the middle lane under the bridge deck, 3m from the mid-span. In order to find the relationship between gross vehicle weight (GVW) and sensor data. Four different types vehicle are used in the test: 1) truck, 2) van, 3) SUV and 4) sedan, which are 9000(lbs.), 5950(lbs.), 4455(lbs.), 4431(lbs.) of GVW, separately. Each vehicle is tested with different moving speed, which are 10 mph , 25mph, and 40 mph. The research team skips traffic time to ensure that only one vehicle passes through the bridge to obtain correct sensing data. The equipment deployment of the field test is shown in **Error! Reference source not found.** and Figure **14**. It is noticed that according to the laboratory test results, due to low-cost cost, draw-wire displacement linear sensor data has low resolution and due to microcontroller natural performance(result is shown in section 5.1). Based on the low-resolution issue, one of the low-cost cost draw-wire displacement linear sensors cannot be applied in a field test.

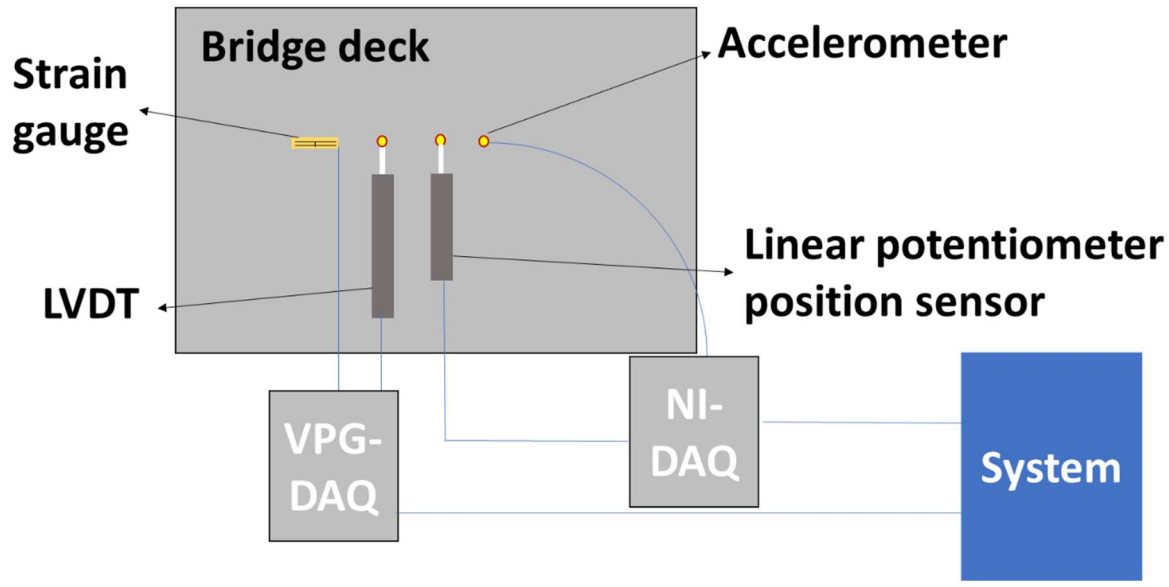


Figure 13. The sensor deployment in the field test

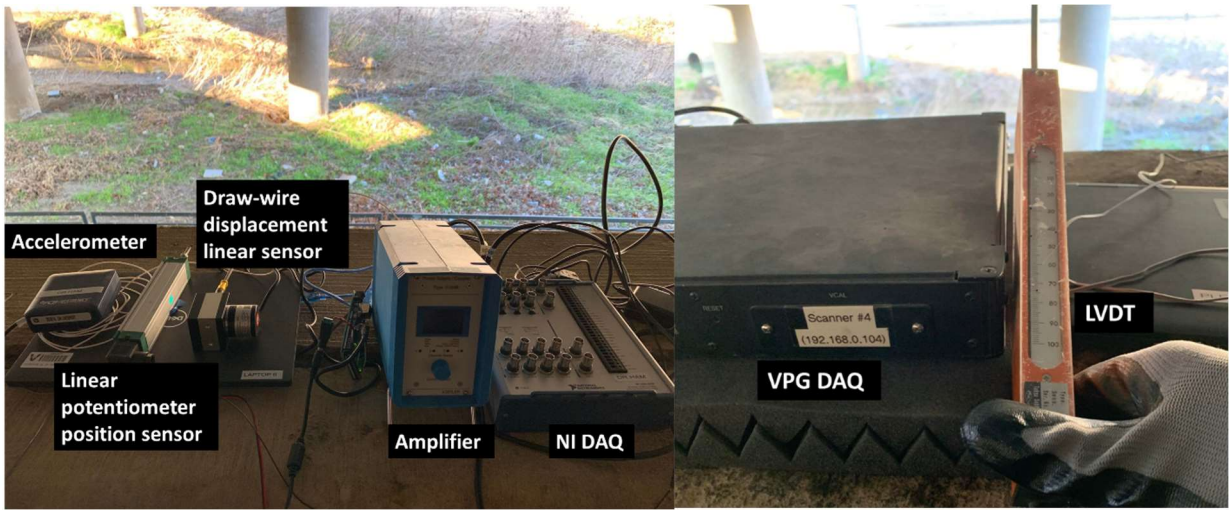


Figure 14. The photo of equipment in the field

### *4.3.2 Finite Element Model*

Depending on the vehicle weight, the FE model design will be slightly different, as shown in

Figure **15**. The design follows the length between the front axle and rear axle. For example, the distance between two axles in truck case is 5.5m, while only 3.9m in SUV. The obtained sensing data will be compared with the FE modeling moving load result after a comprehensive parameter study of FE modeling in section 4.4.

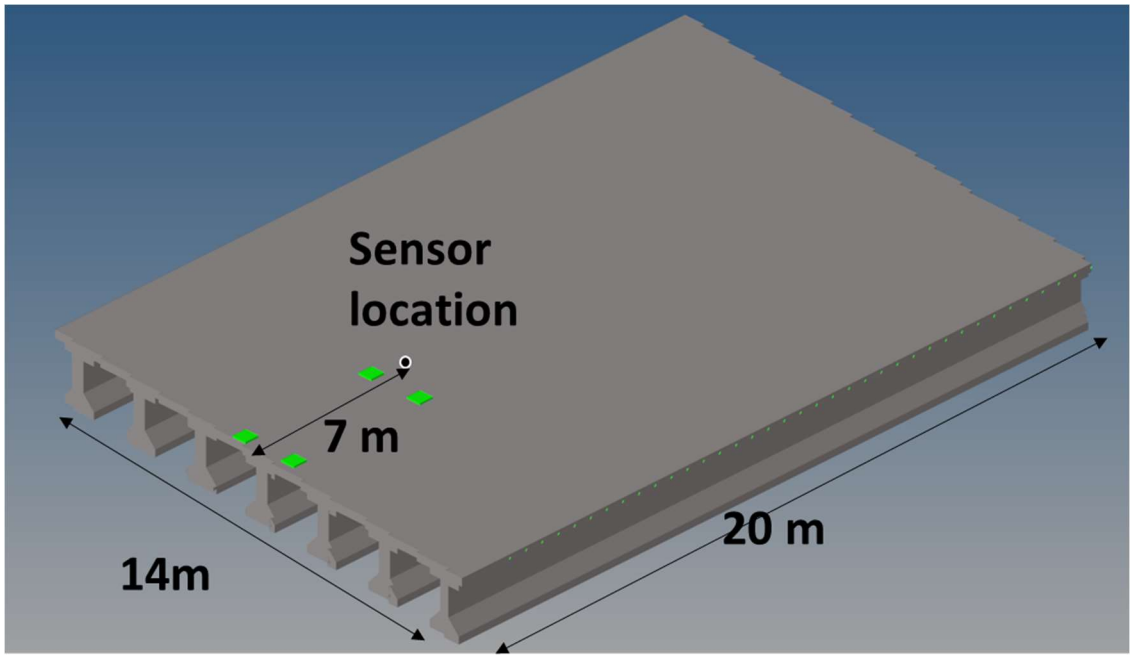

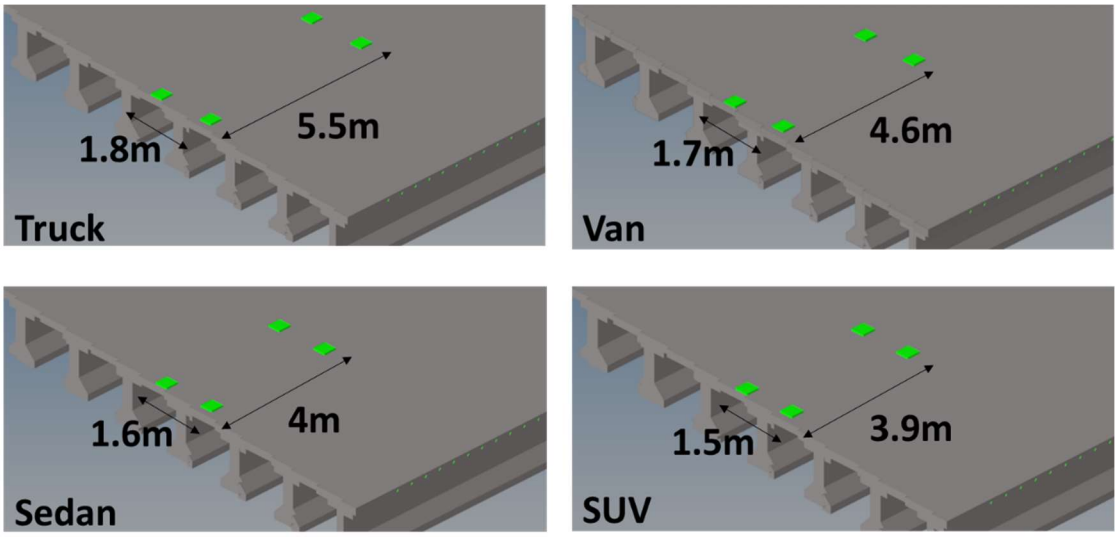


Figure 15. The FE model design and the design between different vehicle

## 4.4 Task5: Finite Element Simulation and Physics-based Structural Model for BWIM Prediction

In Task 5, the FE analysis is performed and comprehensively studied, which includes static load and moving load simulations. The simulation results are proved by vehicle-bridge interaction (VBI) analytical solutions. The physics-based structural model in-depth analysis is discussed below.

### *4.4.1 Finite Element Modeling with Static Load*

The static load FE modeling dimensions is $0.5m \times 15m \times 0.1m$, and there are 30 listening points (L1-L30) arranged under the bridge deck. There are three different crack locations and three different static loads locations, as shown in Figure 16 left. Figure 16 right is the detailed design of cracks, depending on the ratio of the missing element of the cutting section. The mild, moderate, and severe cracks are presented by 10%, 25%, and 45% of the missing elements separately. There are twelve different FE modeling designs for static load conditions, as shown in Figure 17. Three different crack locations with three different load locations as well as three health conditions, a total of 12 models with four damage severity (3 crack locations × three load locations× three crack sizes + 3 healthy conditions without cracks), and 900 sets of data obtained from 30 listening points. Other FE modeling parameters are shown in Table 4, and the explanation for choosing these values is discussed in section 4.4.4 based on parameter study for modeling design. For more realistic FE modeling results, we provide some details of the FE model. If element mesh is designed near crack location, the mesh size should gradually decrease around the crack location since cracks presented by missing elements are "empty" parts in the model. The discontinuously empty parts, especially for the situation of neighbor element size, are big, which brings the other error in ABAQUS: the excitation energy is blocked by an empty part which means the final simulation results of structural response is unreliable with the disconnected signal. Also, ABAQUS has another important design rule; according to the ABAQUS modeling manual, the ratio of mesh size should be maintained

under 5:1 for the FE model subjected to bending and shear deformation. The ratio of mash size over 5:1 may bring the numerical error in ABAQUS calculation.

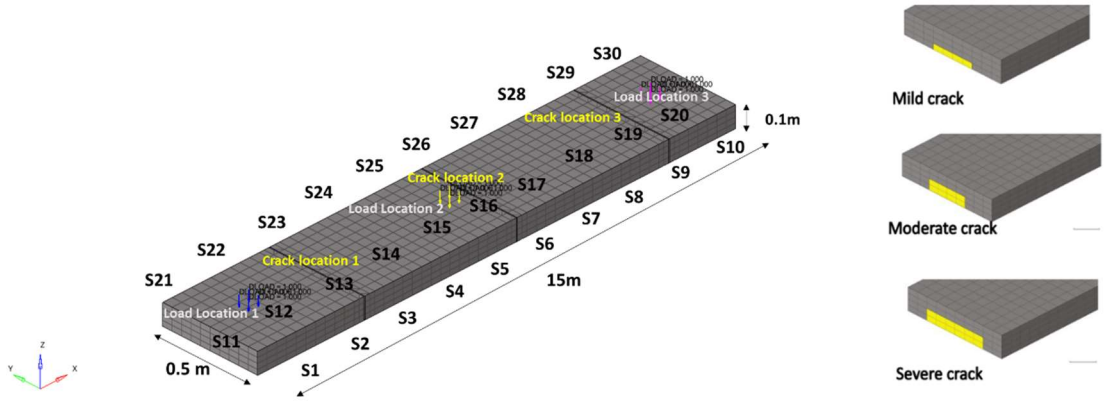


Figure 16. The model of static load design. The static load FE modeling design with three different load locations (LL 1-3) and crack locations (CL1-3). The dimension is 1m×5m×0.02m. There are 30 listening points (L1-L30) deployed under the model. The mild, moderate, and severe cracks are presented by 10%, 20%, and 30% of the missing element.

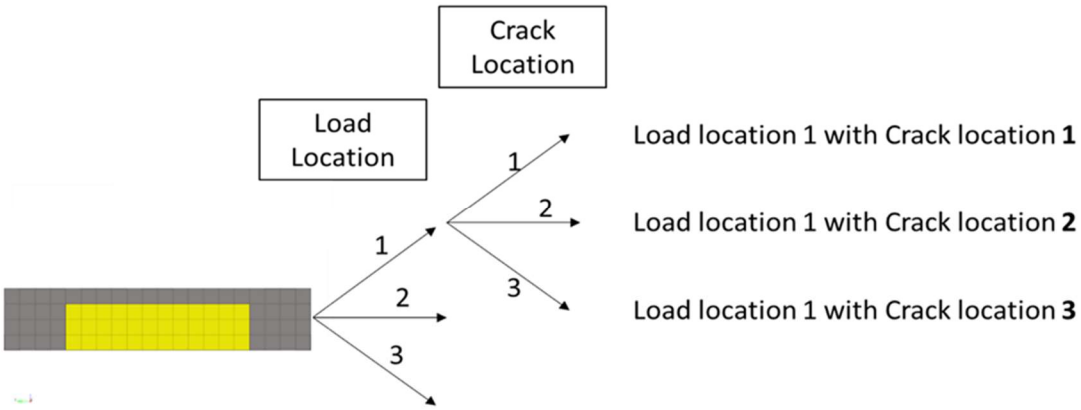


Figure 17. For static load FE modeling design, there are 12 different models based on the combination of different load locations and crack locations (3 crack locations × three load locations + 3 healthy conditions without cracks). In total, there are 12 models and 900 sets of data obtained from 30 listening points.

Table 4. The parameter of the static load model

| LL1 | LL2 | LL3 | CL1 | CL2 | CL3 | Density | Poisson ration | Elastic modulus |
|---|---|---|---|---|---|---|---|---|
| 2(m) | 8(m) | 13(m) | 1(m) | 7.5(m) | 12(m) | 2400 $kg/m^3$ | 0.2 | 30GPa |

### *4.4.2 Finite Element Modeling With Moving Load*

The dimension of the moving load model is the same as the static load model ($0.5m \times 15m \times 0.1m$). The only difference is that the static loads are replaced by the moving loads. The one-way moving load model is shown in Figure 18. The advanced technology called the contact method is used for simulating the actual movement of a vehicle. In the contact method,

the force is transmitting through the contacted surface of two contacted elements. The contacted surface of elements with higher stiffness is named master surface, and the other is named slave surface, such that the direction of transmitting force is always from master surface to slave surface. There are two types of contact conditions between master and slave called contact discretization, one is node-to-surface, and the other is surface-to-surface, as shown in Figure 19 to Figure 22. In the case of node-to-surface contact, as shown in Figure 19(a) each slave node interacts with a point of projection on the master surface, a single slave node interacts with a group of master nodes, the slave node will find the nearest master node and then find the projected slave note on the master surface using interpolation as shown in Figure 19 (b). For linear problems, the transmitted force ($F_N$) is defined by contact stiffness ($k$) and gap ($g_N$) between master and slave as known as clearance in ABAQUS as shown in Figure 20:

$$\boldsymbol{F_N = k \cdot g_N,\ \text{if}\ g_N > 0} \qquad \textbf{Eq.1}$$

and the contact surface should satisfy the equilibrium:

$$\boldsymbol{F_N = \sum_{i=1}^{4} F_{mi}} \qquad \textbf{Eq.2}$$

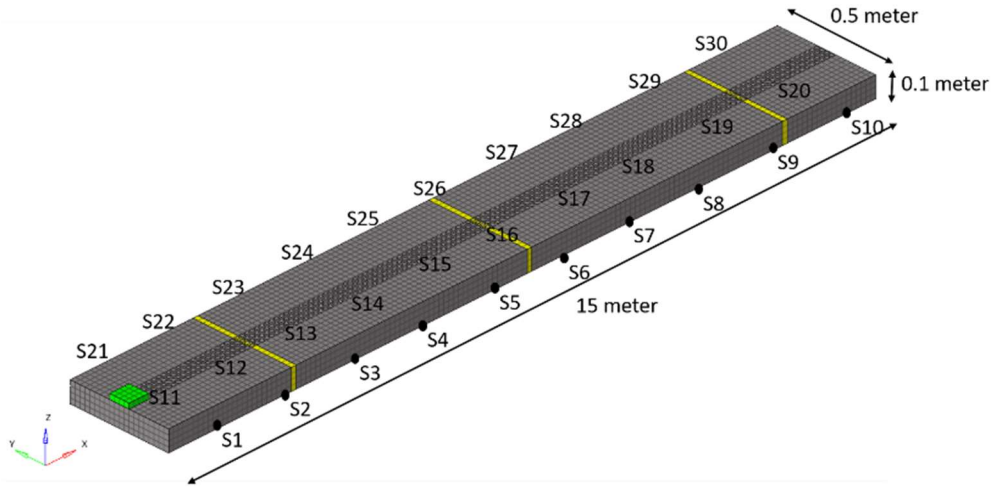


Figure 18. The FE model of the one-way moving load is applied with the contact method.

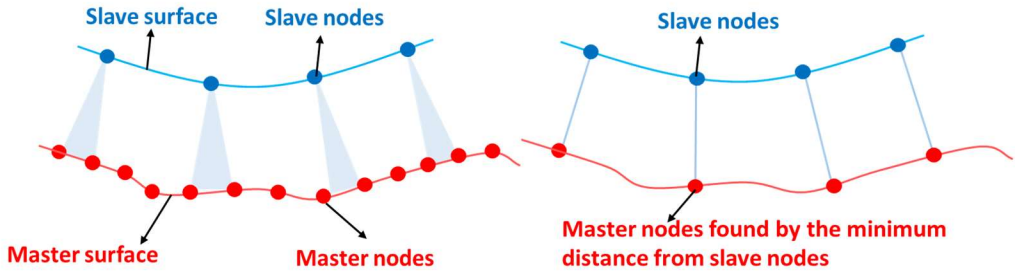


(a) (b)

Figure 19. The concept of note-to-surface contact. Each slave node interacts with a point of projection on the master surface (a), a single slave node interacts with a group of master nodes, the slave node will find the nearest master node and then find the projected slave note on the master surface using interpolation as shown in (b).

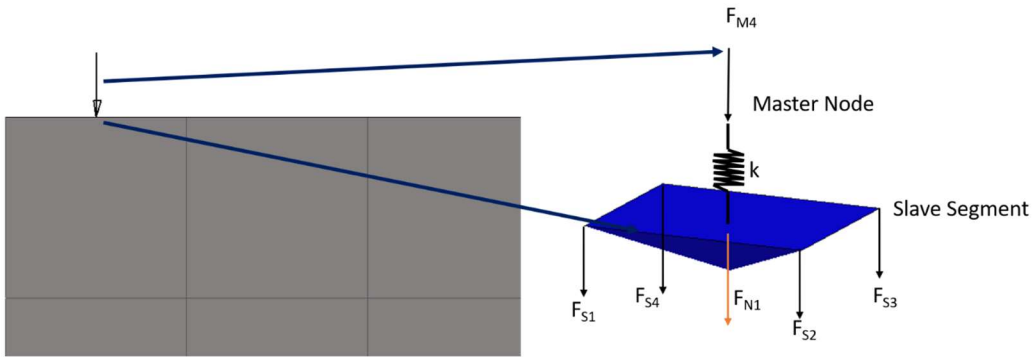


Figure 20. The 3D model of node-to-surface contact in contact method, where $\boldsymbol{F_s}$ and $\boldsymbol{F_M}$ denote the nodal force on slave surface and master surface, k is the contact stiffness between master and slave elements and $\boldsymbol{F_N}$ is equilibrium of forces.

In some cases, a node-to-surface contact can significantly reduce the accuracy of the results. During the modeling of coupled vibrations of an elastic-supported beam and a moving load, a surface-to-surface contact was used [17]. Unlike node-to-surface contact, the surface-to-surface contact uses the average of a projected area on the master surface from each node of slave surface to define the points for contact surface, as shown in Figure 21 and Figure 22.

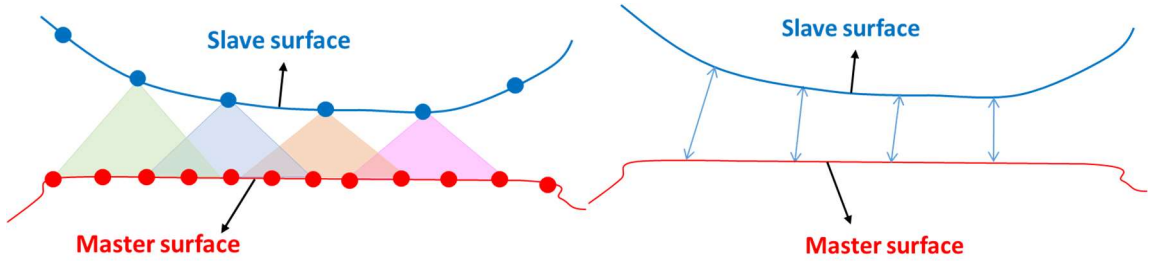


(a) The projected area of the slave surface (b) The average of the projected area

Figure 21. The concept of surface-to-surface contact. It uses the average of the projected area on the master surface from each node of slave surface to define the points for contact surface.

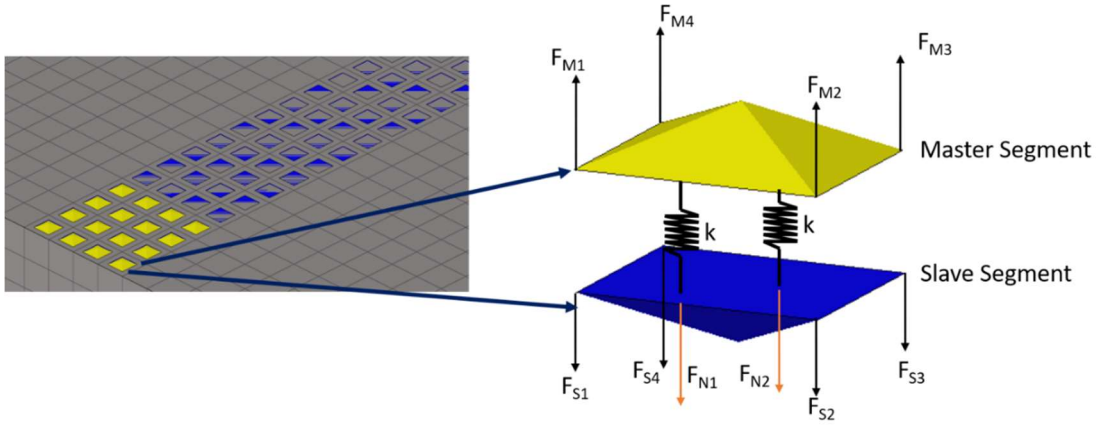


Figure 22. The 3D model of surface-to-surface contact in contact method, where $\boldsymbol{F_s}$ and $\boldsymbol{F_M}$ denote the nodal force on slave surface and master surface, k is the contact stiffness between master and slave elements and $\boldsymbol{F_N}$ is equilibrium of forces.

Compared to the two types of contact discretization, surface-to-surface provides more accurate simulation results because the force can correctly transmit from master to slave. In contrast, node-to-surface can offset the force caused by penetration between master and slave, as shown in Figure 23. Once penetration happened, the penalization, which is the opposite force calculated from contact stiffness $k$ and gap between master and slave $g_N$ may affect simulation results.


(a) Master penetrate into slave ($g_N \neq 0$) (b) Master contact well with slave ($g_N = 0$)

Figure 23. The comparison of two contact discretization. The master may penetrate to slave in note-to-surface contact (a); on the other hand, the master does not penetrate to slave in surface-to-surface contact (b). Once penetration happened, the penalization, which is the opposite force calculated from contact stiffness $\boldsymbol{k_N}$ and gap between master and slave $\boldsymbol{g_N}$ may affect simulation results.

The boundary condition in the contact method called surface interaction defines the surface behavior, including contact damping and friction between the contacted surface. For example, "hard" does not allow transfer of tensile stress across the contacted surface, "linear" and "exponential" provide the contact pressure is a linear or exponential function of the clearance between the surfaces based on the Augmented Lagrangian method [18], [19] and Coulomb's law of friction. Start from Coulomb's law of friction:

$$\boldsymbol{F_f = |t_T| - \mu_f |t_N|} \begin{cases} \boldsymbol{= 0,\ slip} \\ \boldsymbol{< 0,\ stick} \end{cases} \qquad \textbf{Eq. 3}$$

where $F_f$ is friction force, $\mu_f$ is Coulomb's friction coefficient, $t_T$ and $t_N$ are defined as contact stress of normal direction and the tangential direction, separately as shown in Figure 24**Error! Reference source not found.**.

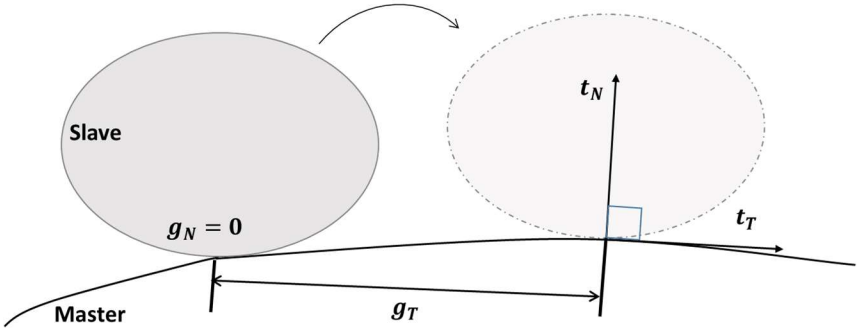


Figure 24. The concept of master and slave contact is in motion. $\boldsymbol{g_N}$ is the gap between master and slave, $\boldsymbol{g_T}$ is the distance between slaves in motion, and $\boldsymbol{t_N}$, $\boldsymbol{t_T}$ displays normal contact stress and tangential contact stress.

Consider two bodies in contact, a master and a slave body. The normal contact stress $t_N$ precludes penetration of the contacting bodies by imposing $g_N = 0$, whereas the tangential contact stress $t_T$ follows Coulomb's rule such that the stick-slip constraints are satisfied. Thus, the equation of the Lagrangian method considered Coulomb's law of friction:

$$\boldsymbol{t_N = \epsilon_N g_N + \lambda_N \text{ and } t_T = \bar{\epsilon}_T g_T + \lambda_T} \qquad \textbf{Eq. 4}$$

where $\epsilon_N$"1 is a strictly positive normal penalization parameter, $\lambda_N$ is normal augmented Lagrange multiplier, $\bar{\epsilon}_T$ is tangential penalization parameter that returns a stickily positive penalty number $\epsilon_T$"1 in stick situation and 0 in slip situation and $\lambda_T$ is tangential augmented Lagrange multiplier. Penalization parameter is calculated from the situation when the master penetrates into the slave; this value is equal to the contact stiffness ($k_N$) times the penetration distance ($g_N$), as shown in Figure 24 (a). More derivation of contact method [18], [20]. The transmitting force is automatically calculated by the Augmented Lagrangian method by giving the contact condition such as contact discretization and surface interaction property. This force is used to simulate moving load by giving direction and velocity—the parameter setting for the contact method to simulate one-way moving load, as shown in Table 5.

Table 5. The parameter setting for contact method to simulate one-way moving load

| Velocity | Concrete Density | Concrete Poisson ratio | Concrete Elastic modulus | Tyre Density | Tyre Poisson ratio | Tyre Elastic modulus | Load Applied |
|---|---|---|---|---|---|---|---|
| 6mph | 2400 kg/m$^3$ | 0.2 | 30GPa | 700 kg/m$^3$ | 0.3 | 1GPa | 1Hz |

### *4.4.3 Analytical Solutions:*

The VBI analytical solutions are proposed to verify FE simulation results introduced in section 4.4.2. The concept of VBI is based on the interdependence between moving vehicles and bridge response. The comprehensive parameter study for FE simulation results is proved by analytical solutions based on the maximum displacement energy loss (%), which demonstrates the feasibility of using the contact method to simulate moving vehicles in FE simulation. In order to comprehensively compare and verify the FE simulation results of moving loads, the detail of the analytical solution is described below. The model considered a passing vehicle and simple bridge, which is shown in **Error! Reference source not found.**, where L is the length of the bridge, $E, I$, $\omega_b$ are bridge modulus of elasticity, bridge second moment of area and bridge first natural frequency, and $m_v$ , $k_v$ , $\omega_v = \sqrt{k_v/m_v}$ are mass of vehicle, vehicle first natural frequency, and vehicle stiffness, separately.

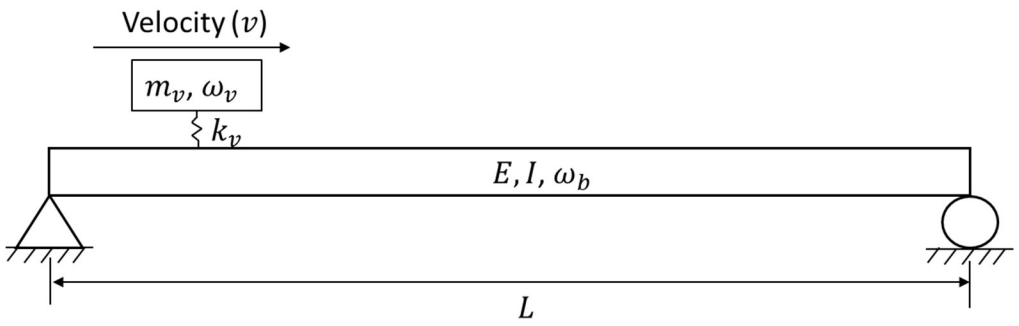


Figure 25. The simple model considered passing vehicle and bridge, where L is the length of the bridge, $\boldsymbol{E, I}$, $\boldsymbol{\omega_b}$ are bridge modulus of elasticity, bridge second moment of area and bridge first natural frequency, and $\boldsymbol{m_v}$ , $\boldsymbol{k_v}$ , $\boldsymbol{\omega_v = \sqrt{k_v/m_v}}$ are mass of vehicle, vehicle first natural frequency, and vehicle stiffness, separately.

The equation of motion for the moving mass over beam can be written as(Yang et al., 2004; E. J. OBrien et al., 2017):

$$\ddot{q}_v(t) = \frac{\Delta_{st}\omega_v^2}{2(1-s^2)}\left[A_1 cos\omega_v t + A_2 cos\frac{2\pi vt}{L} + A_3\, cos\left(\omega_b - \frac{\pi v}{L}\right)t + A_4\, cos\left(\omega_b + \frac{\pi v}{L}\right)t\right] \quad \textbf{Eq. 5}$$

and the first mode structural response of bridge can be expressed as:

$$u(x,t) = \sum \frac{\Delta_{st}}{1-s^2}\left\{sin\left(\frac{\pi x}{L}\right)\left[sin\left(\frac{\pi vt}{L}\right) - s \cdot sin\,(\omega_b t)\right]\right\} \quad \textbf{Eq. 6}$$

$$\ddot{u}(x,t) = \sum \frac{\Delta_{st}}{1-s^2}\left\{sin\left(\frac{\pi x}{L}\right)\left[(\omega_b^2 \cdot s)\, sin(\omega_b t) - (\frac{\pi v}{L})^2 \cdot sin\,(\frac{\pi vt}{L})\right]\right\} \quad \textbf{Eq. 7}$$

where $\ddot{q}_v(t)$ is the acceleration of vehicle at the moment $t$; $u(x,t)$ and $\ddot{u}(x,t)$ are displacement and acceleration of the bridge with a specific location($x$) and time($t$); $\Delta_{st}$ is the approximate static deflection at the mid-span of the beam under gravity action of $m_v$; $s$ is bridge coefficient related with bridge properties; and $A_1$, $A_2$, $A_3$, $A_4$determine the relative contributions of each component to the total acceleration response. The expression of these parameters:

$$\Delta_{st} = -\frac{2m_v g L^3}{\pi^4 EI},\ s = \frac{\pi v}{L\omega_b} \quad \textbf{Eq.8}$$

$$A_1 = 1 - \frac{1}{1-(2\mu s)^2} - \frac{s}{1-\mu^2(1-s)^2} + \frac{s}{1-\mu^2(1+s)^2} \quad \textbf{Eq.9}$$

$$A_2 = \frac{(2\mu s)^2}{1-(2\mu s)^2} \quad \textbf{Eq. 10}$$

$$A_3 = \frac{\mu^2 s(1-s)^2}{1-\mu^2(1-s)^2} \quad \textbf{Eq.11}$$

$$A_4 = -\frac{\mu^2 s(1+s)^2}{1-\mu^2(1+s)^2} \quad \textbf{Eq.12}$$

According to **Error! Reference source not found.**, the displacement and acceleration of the bridge are dominated by driving frequency $\left(\frac{v}{L}\right)$ and bridge natural frequency ($\omega_b$). On the other hand, the **Error! Reference source not found.** for presenting the vehicle acceleration is

dominated by driving frequency$\left(\frac{v}{L}\right)$, bridge natural frequency ($\omega_b$), and vehicle natural frequency ($\omega_v$). It could be break down as:

$$\ddot{q}_{v,freq}(t) = \frac{\Delta_{st}\omega_v^2}{2(1-s^2)} A_1 cos\omega_v t \quad \textbf{Eq.13}$$

$$\ddot{q}_{v,speed}(t) = \frac{\Delta_{st}\omega_v^2}{2(1-s^2)} A_2 cos\frac{2\pi v t}{L} \quad \textbf{Eq.14}$$

$$\ddot{q}_{b,freq}(t) = \frac{\Delta_{st}\omega_v^2}{2(1-s^2)} \left[A_3 cos\left(\omega_b - \frac{\pi v}{L}\right)t + A_4 cos\left(\omega_b + \frac{\pi v}{L}\right)t\right] \quad \textbf{Eq.15}$$

where $\ddot{q}_{v,freq}(t)$ is the component related to the vehicle's natural frequency ($\omega_v$), $\ddot{q}_{v,speed}(t)$ is the part related to driving frequency $\left(\frac{v}{L}\right)$ and $\ddot{q}_{b,freq}(t)$ is the part related to the bridge's natural frequency. The unit of input for properties is shown in Table 6.

Table 6. The properties of a bridge and moving vehicle

| Properties | Unit | Symbol |
|---|---|---|
| Length | $m$ | $L$ |
| Mass of bridge | $kg$ | $m$ |
| Modulus of elasticity | N/$m^2$ | $E$ |
| The first moment of area | $kg - m^2$ | $I$ |
| First natural frequency | $Hz$ | $\omega_b$ |
| Mass of vehicle | $kg$ | $m_v$ |
| Speed of vehicle | $m/s$ | $v$ |
| Stiffness of vehicle | $N/m$ | $k_v$ |

### *4.4.4 Parameter Study (In-depth Research of Physics-based Model)*

In this section, several parameters in the FE model are comprehensively studied for finding the better model design, including 1) Elastic modulus of a bridge, 2) density of bridge, 3) mesh size, 4) depth and width of the bridge. The bridge design of the parameter study is shown Table 7, which includes width (b), depth (H), density (D), elastic modulus (E), and mesh size. The model detail is shown in Figure 26 to Figure 28. Finally, the results of parameter studies are compared with bridge displacement from analytical solutions, which are discussed in section 4.2 to verify the accuracy of the FE model design.

Table 7. The bridge design of parameter study, which including width (b), depth (h), volume (V), the first moment of inertia(I), density (D), mass(m), elastic modulus (E), and mesh size.

| | b | h | V | I | D | m | E | mesh |
|---|---|---|---|---|---|---|---|---|
| E=30GPa | 0.5 | 0.1 | 0.75 | 4.16667E-05 | 2400 | 1800 | 30GPa | 0.1 |
| E=33GPa | 0.5 | 0.1 | 0.75 | 4.16667E-05 | 2400 | 1800 | 33Gpa | 0.1 |
| E=35GPa | 0.5 | 0.1 | 0.75 | 4.16667E-05 | 2400 | 1800 | 35Gpa | 0.1 |
| E=38GPa | 0.5 | 0.1 | 0.75 | 4.16667E-05 | 2400 | 1800 | 38Gpa | 0.1 |
| E=41GPa | 0.5 | 0.1 | 0.75 | 4.16667E-05 | 2400 | 1800 | 41Gpa | 0.1 |
| Density100 | 0.5 | 0.1 | 0.75 | 4.16667E-05 | 100 | 75 | 30GPa | 0.1 |
| Density1000 | 0.5 | 0.1 | 0.75 | 4.16667E-05 | 1000 | 750 | 30GPa | 0.1 |
| Density2400 | 0.5 | 0.1 | 0.75 | 4.16667E-05 | 2400 | 1800 | 30GPa | 0.1 |
| Density3000 | 0.5 | 0.1 | 0.75 | 4.16667E-05 | 3000 | 2250 | 30GPa | 0.1 |
| Density6000 | 0.5 | 0.1 | 0.75 | 4.16667E-05 | 6000 | 4500 | 30GPa | 0.1 |
| Depth 0.1 | 0.5 | 0.1 | 0.75 | 4.16667E-05 | 2400 | 1800 | 30GPa | 0.1 |
| Depth 0.2 | 0.5 | 0.2 | 1.5 | 0.000333333 | 2400 | 3600 | 30GPa | 0.1 |
| Depth 0.3 | 0.5 | 0.3 | 2.25 | 0.001125 | 2400 | 5400 | 30GPa | 0.1 |
| Depth 0.4 | 0.5 | 0.4 | 3 | 0.002666667 | 2400 | 7200 | 30GPa | 0.1 |
| Depth 0.5 | 0.5 | 0.5 | 3.75 | 0.005208333 | 2400 | 9000 | 30GPa | 0.1 |
| width 0.1 | 0.1 | 0.1 | 0.15 | 8.33333E-06 | 2400 | 360 | 30GPa | 0.1 |
| width 0.3 | 0.3 | 0.1 | 0.45 | 0.000025 | 2400 | 1080 | 30GPa | 0.1 |
| width 0.5 | 0.5 | 0.1 | 0.75 | 4.16667E-05 | 2400 | 1800 | 30GPa | 0.1 |
| width 0.7 | 0.7 | 0.1 | 1.05 | 5.83333E-05 | 2400 | 2520 | 30GPa | 0.1 |
| width 1.3 | 1.3 | 0.1 | 1.95 | 0.000108333 | 2400 | 4680 | 30GPa | 0.1 |
| width 2.5 | 2.5 | 0.1 | 3.75 | 0.000208333 | 2400 | 9000 | 30GPa | 0.1 |
| Mesh 0.1x0.1 | 0.5 | 0.1 | 0.75 | 4.16667E-05 | 2400 | 1800 | 30GPa | 0.1x0.1 |
| Mesh 0.05x0.05 | 0.5 | 0.1 | 0.75 | 4.16667E-05 | 2400 | 1800 | 30GPa | 0.05x0.05 |
| Mesh 0.025x 0.025 | 0.5 | 0.1 | 0.75 | 4.16667E-05 | 2400 | 1800 | 30GPa | 0.025x0.025 |

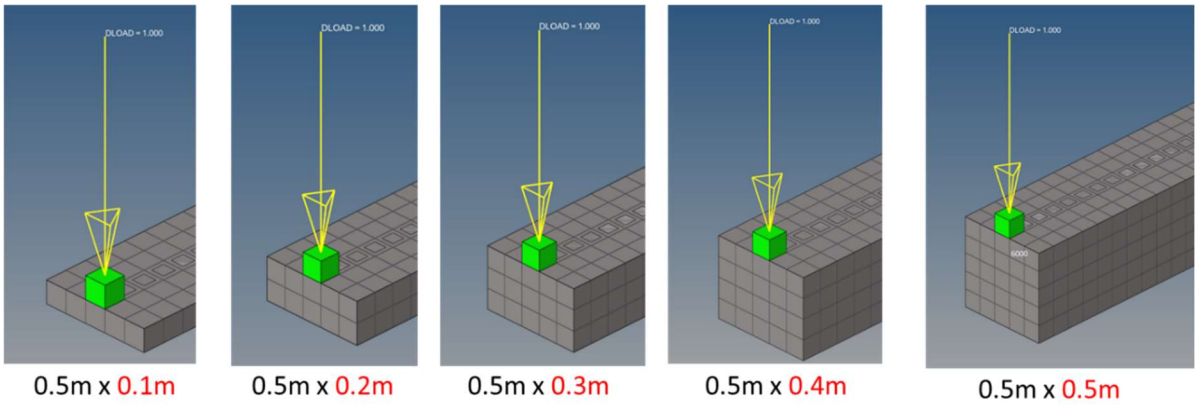


Figure 26. The models for depth(h) parameter study with five different depths: 0.1, 0.2, 0.3, 0.4, and 0.5m.

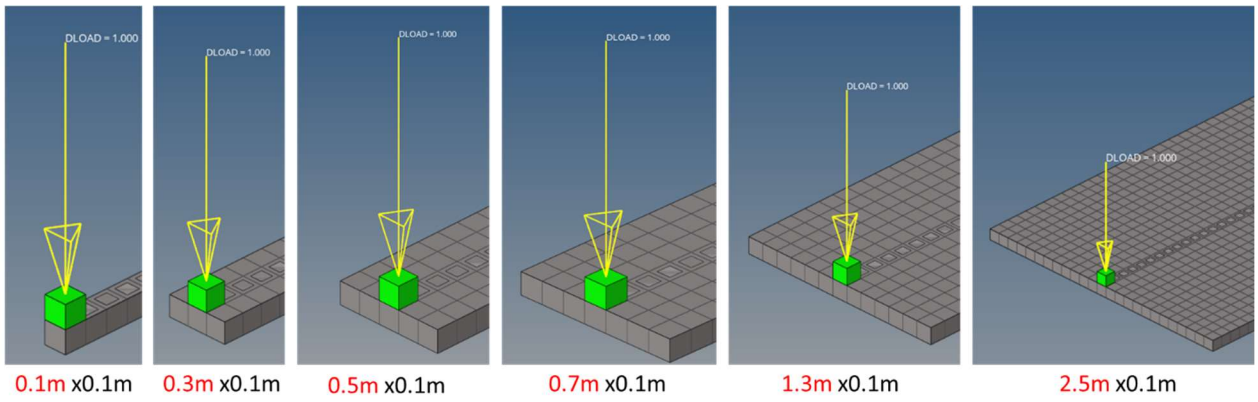


Figure 27. The models for width(b) parameter study with six different widths: 0.1, 0.3, 0.5, 0.7,1.3 and 25m.

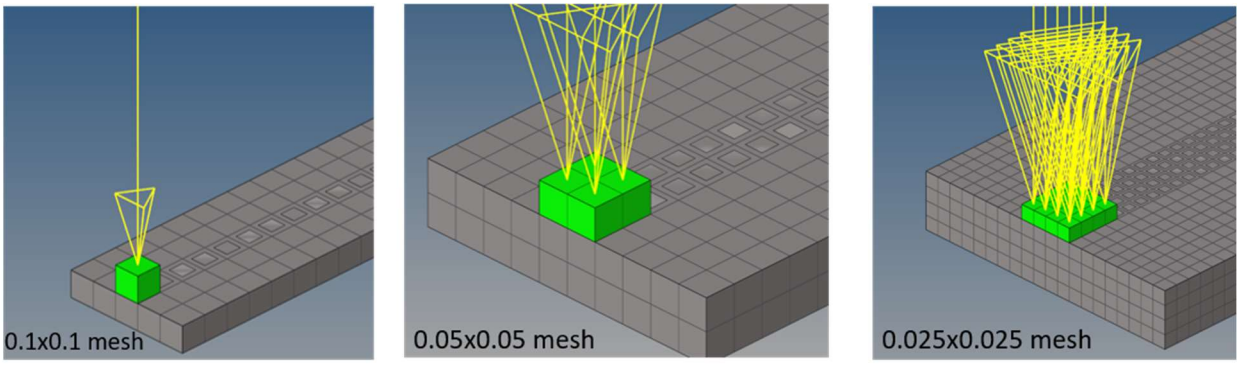


Figure 28. The models for mesh size parameter study with three different mesh sizes: 0.1, 0.05, and 0.025m mesh.

## 4.5 Task6: Data Analysis Deploying Deep Learning Neural Network (DLNN) of Real-time BWIM prediction models

In these years, the influence of information technology (IT) has grown tremendously regarding all different aspects of today's society. One of the most well-known IT is ML. ML is the field of computer science that uses statistical techniques to enable computers to act and make data-driven decisions and progressively learn and improve over time without being explicitly programmed. The outcome of ML is also remarkable, and the performance is even superior to human intelligence. The input of the ML model is called a feature, which displays the importance of variables is known as structural responses from FE simulation. For the process in damage prediction, it is unnecessary to use all simulation results as a feature because some variables (e.g., displacement) may not provide a significant difference between healthy and damaged conditions. Moreover, the more features are used, the more computing time, and also may get inaccurate prediction results caused by overfitting. To improve the accuracy of a prediction model, data selection is used for raking the importance regarding prediction results.

### *4.5.1 Data Feature and Feature Selection*

Data features that show the important part of data is required for the ML model; they are extracted from structural responses from FE simulation results. These features are used to train the ML model for damage prediction. The features included the statistical indicator of structural response (e.g., acceleration, stress, displacement, and spectrum analysis from *fast Fourier transform*), and also considered these structural responses as a feature directly—the statistical indicator as shown in Table 8.

Table 8. Statistical indicator and FE modeling information used for data features [23]

| Peak | Mean | Mean square | Root mean square | Variance |
|---|---|---|---|---|

| | | | | |
|---|---|---|---|---|
| $max\|x\|$ | $\frac{1}{n}\sum_{i=1}^{n} x_i$ | $\frac{1}{n}\sum_{i=1}^{n} (x_i)^2$ | $\sqrt{\frac{1}{n}\sum_{i=1}^{n} (x_i)^2}$ | $\frac{1}{n}\sum_{i=1}^{n} (x_i - \bar{x})^2$ |
| Standard deviation | Skewness | Kurtosis | Crest factor | K-factor |
| $\sqrt{\frac{1}{n}\sum_{i=1}^{n} (x_i - \bar{x})^2}$ | $\frac{\frac{1}{n}\sum_{i=1}^{n}(x_i - \bar{x})^3}{\sigma^3}$ | $\frac{\frac{1}{n}\sum_{i=1}^{n}(x_i - \bar{x})^4}{\sigma^4}$ | $\frac{x_{peak}}{x_{rms}}$ | $x_{peak} \cdot x_{rms}$ |

The statistical method called feature selection is applied to rank the positive correlation between features and predict results for choosing the most available feature. The irrelevant and redundant features are filtered by using feature selection. Feature selection is not only used to simplify the ML model to avoid overfitting (which may bring unreasonable predicted results while increasing the accuracy of the model), but it also decreases the computing time in the data training process. There are two commonly used approaches for data selection: filter and embedded. The filter approach is used to measure feature importance based on the characteristics of the features by calculating the statistical indicator of data, as shown in Table 8. The feature will be removed if the feature has a low correlation with data. The most commonly used statistical criteria method is Pearson's correlation. This criteria method is used for finding the relationship between two quantities by using the following equation [24]:

$$PC(x,y) = \frac{\sum_i (x_i - \bar{x})(y_i - \bar{y})}{\sqrt{\sum_i (x_i - \bar{x})^2 (y_i - \bar{y})^2}} \quad \text{Eq.16}$$

where $x$ and $y$ are two independent features. $PC(x,y)$ value lies between [-1,1], which presents the features as a negative correlation or positive correlation. In the case of 0, there is no correlation between features.

For the embedded approach, this approach is incorporated with other ML algorithms (e.g., random forest) to calculate the weight of features. The random forest composed of several decision trees is shown in Figure 29. Each decision tree can calculate the impurity based on randomly picking features and giving the weight for each feature depending on their importance, which is known as the positive correlation between features and predicted results. The classification results of each decision tree are summarized based on their weight as a random forest output. The four commonly used types of impurity are shown in Table 9. This paper uses an embedded approach with the random forest for feature selection since random forest calculates the importance, known as the weight of features, from the number of decision trees to provide more reliable output.

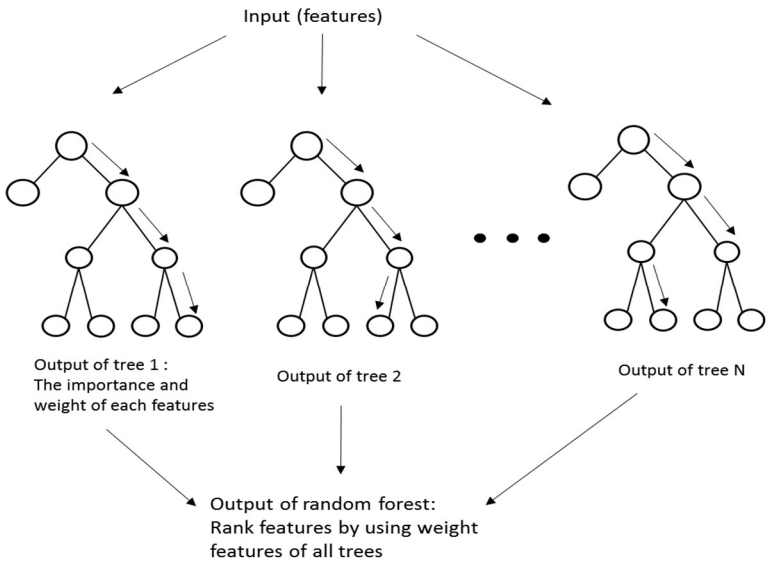


Figure 29. The concept of random forest. The random forest comprises several decision trees that randomly pick features as input calculated by impurity, as shown in **Error! Reference source not found.**. The output of random forest depends on the feature of each tree.

Table 9. Four commonly used impurities in random forest

| Gini impurity | Entropy | Mean Square Error(MSE) | Mean Absolute Error(MAE) |
|---|---|---|---|
| $\sum_{i=1}^{n} x_i(1-x_i)$ | $\sum_{i=1}^{n} -x_i \log_2 x_i$ | $\frac{1}{n}\sum_{i=1}^{n}(x_i-\bar{x})^2$ | $\frac{1}{n}\sum_{i=1}^{n}\lvert x_i-\bar{x}\rvert$ |

### *4.5.2 Damage Prediction Methods*

For finding reliable damage prediction results, several different ML technology are applied: 1) backpropagation propagation (BP), 2) support vector machine (SVM), 3) decision tree (DT), and 4) XGBoost. The data from FE simulation are used as training data for the ML model. The ML model is trained with 70% of the simulation results, and the other 30% is used for damage prediction.

#### Backpropagation (BP)

Backpropagation(BP) algorithm is one of the most commonly used artificial neural networks (ANN), the simple neural network as known as multilayer perceptron(MLP), as shown in Figure 30, where $\delta_i$ presenting error of each neurons calculated with data information (e.g., structural response or statistical indicator), $x_i$ is input data as known as structural response and $f(x_i)$ is output of each neurons to show the classified results as known as the damage severity in this project. In BP, the error of each neuron is re-calculated in the "back direction" to improve the

accuracy of prediction results[25]. For example, the first error is calculated from left to right (e.g., $\delta_1$ to $\delta_4$ to $\delta_8$ to $\delta_{10}$ in Figure 17), and then the updated error is recalculated from right to left based on the first calculated error (e.g., new $\delta_8$ is recalculated from $\delta_{10}$). The equation for updating error as shown in **Error! Reference source not found.**:

$$\boldsymbol{\delta_i = f(x_i)(1 - f(x_i))} \ \boldsymbol{\sum_{k \in \, next\ layer\ neuron} W_{k,i}\delta_k} \qquad \textbf{Eq. 17}$$

Similar concept for recalculating weight between neurons, weight is updated by using new $\delta_i$ and loss function (e.g., mean square error of features),

$$\boldsymbol{\frac{\partial\,(Loss\ function)}{\partial w_i} = \delta_i f(x_{i-1}))^{\,T}} \qquad \textbf{Eq. 18}$$

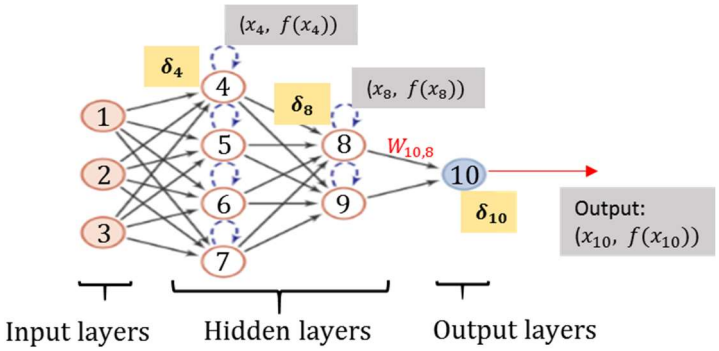


Figure 30. The multilayer perceptron explains the backpropagation neural network. $\boldsymbol{\delta_i}$ presenting error between neuron, $\boldsymbol{t_i}$ is input data of each neuron and $\boldsymbol{f(x_i)}$ is output of each neuron. The error of each neuron is re-calculated in the "back direction" to improve the accuracy of prediction results. For example, the first error is calculated from left to right (e.g., $\boldsymbol{\delta_1}$ to $\boldsymbol{\delta_4}$ to $\boldsymbol{\delta_8}$ to $\boldsymbol{\delta_{10}}$), and then the updated error is recalculated from right to left based on the first calculated error(e.g., new $\boldsymbol{\delta_8}$ is recalculated from $\boldsymbol{\delta_{10}}$). Similar concept for recalculating weight between neurons, weight is updated by using new $\boldsymbol{\delta_i}$.

## Support vector machine (SVM)

SVM is an algorithm used to classify or regress for features. Similar to the regression curve, the border called hyperplane divides two different classes of data. SVM is used to find the optimized hyperplane with the largest margin range. The simple concept is shown in Figure 31. The goal is to find an optimized hyper-plane that has a maximum margin range, the distance between any point in space $x$ to hyper-plain ($w^T x + b = 0$) [26] is:

$$\boldsymbol{d = \frac{|w^T x + b|}{\|w\|}} \qquad \textbf{Eq.19}$$

where $w$ is the normal vector of hyper-plane and b is the intercept of hyper-plane. The maximum of margin range $\gamma$ can be expressed:

$$\gamma = 2 * min(d) = \frac{2}{\|w\|} \quad \textbf{Eq.20}$$

Thus, the optimized hyper-plane, which has the largest margin range, defines the best classification border of data, as shown in Figure 31.

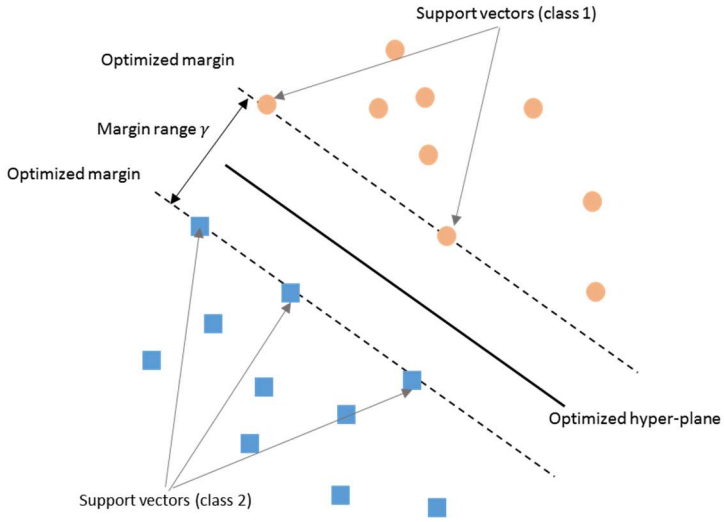


Figure 31. The concept of SVM. The distance between features and hyper-plane can calculate the optimized hyper-plane with the maximum margin range. The optimized hyper-plane has a maximum margin range, which defines the best classification border of features. Therefore, the optimized hyper-plane can classify features with high accuracy.

## Decision Tree (DT)

Decision tree (DT) is an optimized regression method presenting by tree structure where each node displays one attribute, each branch displays one decision, and each leaf indicates one outcome, as shown in Figure 32. The algorithm makes the decision in each node depends on the threshold, as known as information entropy. The definition of information entropy:

$$\boldsymbol{Entropy}(x) = -\sum_{n=1}^{K} x_n \, log_2 \, x_n \quad \textbf{Eq. 21}$$

where $x$ is a dataset of features, n is the subset of features that have similar attributes, $x_n$ is the ratio between n of all data and K is the classes of features (e.g., for binary yes/no question, K=2). Based on the attribute of features and threshold calculated from entropy, the features will be classified into different branches and leaves in different classes to give the optimized classification: the lower the entropy value, the more similar the features in the dataset ($x$).

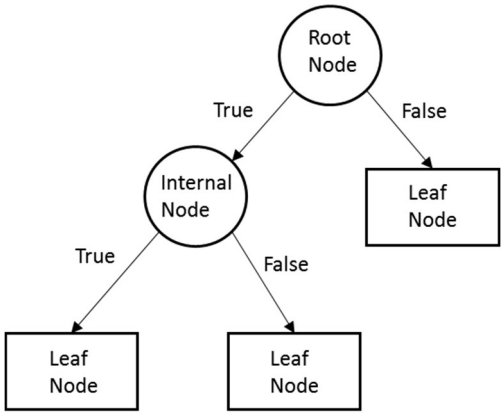


Figure 32. The simple binary decision tree model. Each node displays one attribute, each branch displays one decision based on the entropy threshold calculated in nodes, and each leaf indicates one output.

## XGBoost

XGBoost is known as Extreme gradient boosting, which combined the benefits of tree boosting and tree assemble. Tree boosting, known as gradient boosting, is used to find the best answer with the lowest error by using the loss function (e.g., mean square error). More detail regarding gradient boosting in [27]. The tree assembles mean considering the results from all decision trees to vote(or sum) the output with the highest score(e.g., weight)—the simple model of XGBoost with tree ensemble concept as shown in **Error! Reference source not found.**[28]. Similar to a decision tree, in the tree ensemble, each tree has its own threshold (e.g., entropy) in nodes to classify data, and the final prediction is based on the sum of predictions from each tree. In XGBoost, the first and second-order derivative of Taylor polynomial is used for finding the best prediction results; more detail goes to [28]. By comparing all prediction results from each tree, XGBoost can provide more accurate prediction results.

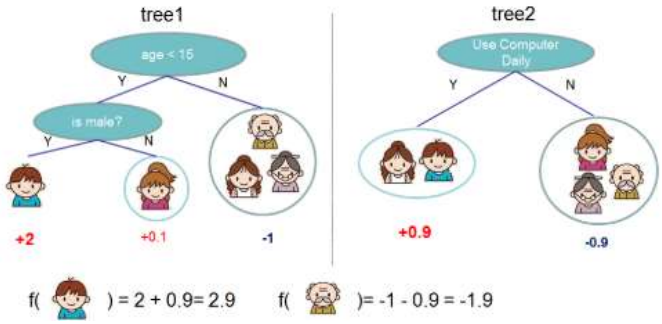


Figure 33. XGBoost model with tree ensemble. The final prediction is the sum of predictions from each tree[28].

# 5. ANALYSIS AND FINDINGS

## 5.1 The First Laboratory (Small-scale)

The first laboratory test is to study sensor performance and sensitivity under simulated vehicle movement. There are three displacement data, one acceleration data, and strain data. Two example results are shown in Figure **34**. According to Figure **34** (a), LVDT gives the maximum amplitude data with proper resolution, which can record continuously changed data over time. The low-cost linear potentiometer or position sensor also resent good resolution. The displacement value is slightly different from the result of LVDT since the movable steel bar in linear position sensor only can be pushed or pulled by bridge deck displacement, while LVDT has an additional spring that can push the pointer back. For the low-cost draw-wire displacement linear sensor, the data resolution is only 0.1(mm), which cannot detect all displacement variation lower than 0.1mm. Thus, the signal resents the time-step signal. Considering that the displacement in the field test may be lower than lab test, the research team decided to not apply low-cost draw-wire displacement linear sensor in a field test. According to Figure **34** (b and c), the strain data happened when acceleration goes to a higher amplitude, from 1000 to 2000 samples window. Normally acceleration happens at the moment when load act on the concrete, while displacement increases when a wheel goes to the middle point of the specimen.

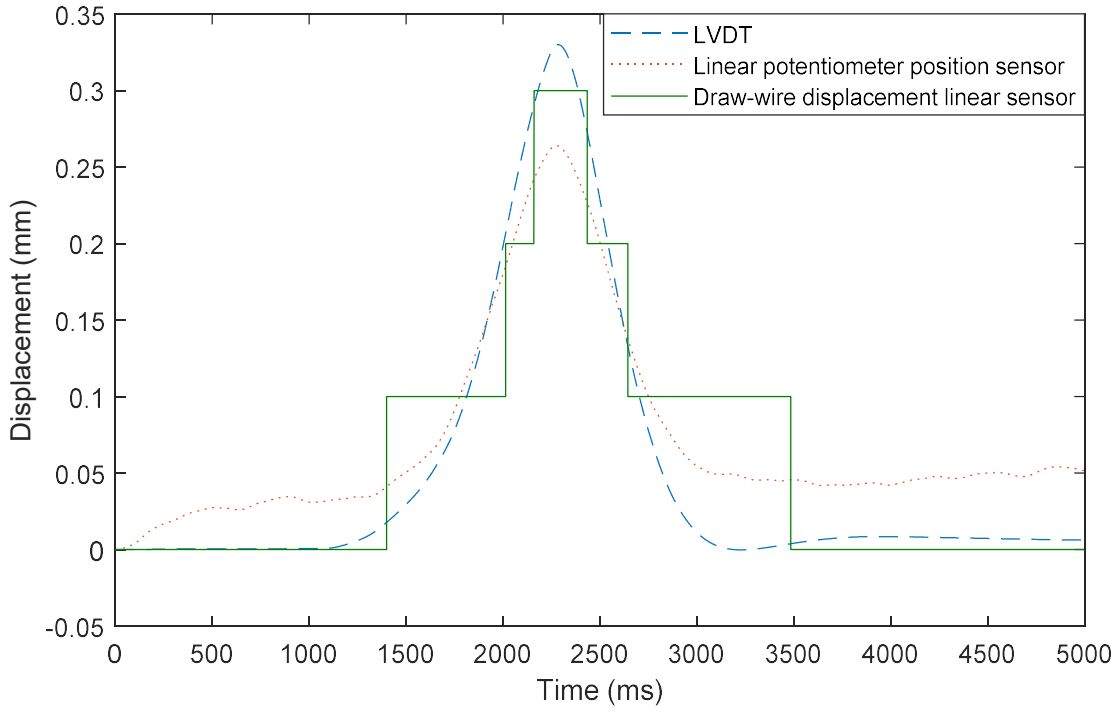


**(a)**

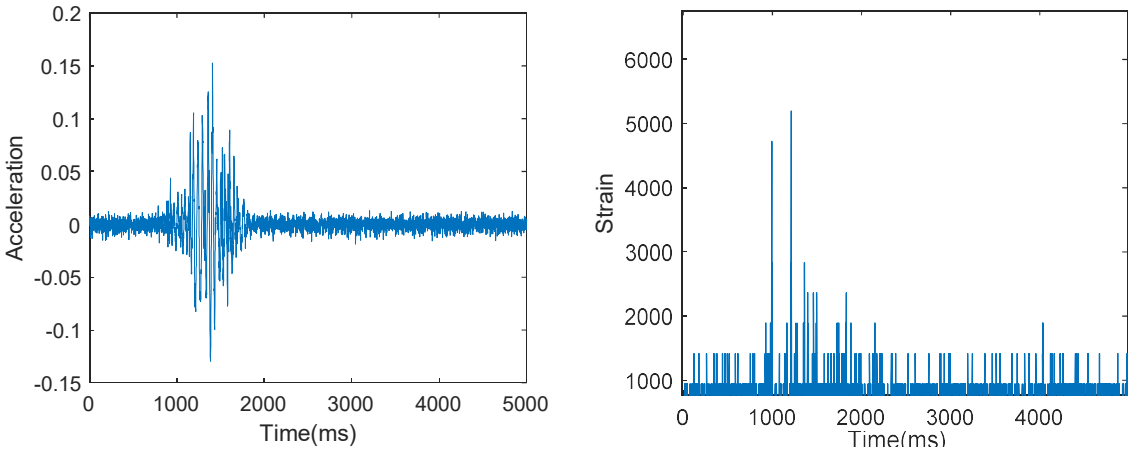


**(b)** **(c)**

Figure 34. The example of the first laboratory test. Displacement(a), acceleration(b) and strain(n). According to a, LVDT gives the maximum amplitude data with a good resolution which can be record continuously changed data by time. For the low-cost draw-wire displacement linear sensor, the data resolution only 0.1(mm).

## 5.2 The Second Laboratory (Big-scale)

From the first laboratory test, LVDT demonstrates the best resolution for all displacement sensors. Thus we decide to use LVDT data as an important reference to verify FE simulation results and other field testing results. The comparison deflection results between the second laboratory test with FE simulation as shown in Figure 35. The x-axis deflection of the mid-span sensor, and the y-axis is load. This figure only records the concrete beam deflection before it fractures. According to Figure 35, both simulation and experiment show the same pattern when a load is increasing. When load up to 400kN, the deflection in both cases is faster increased. Note that a load of this FE simulation model uses static load simulation. Moving load is applied with the field test model.

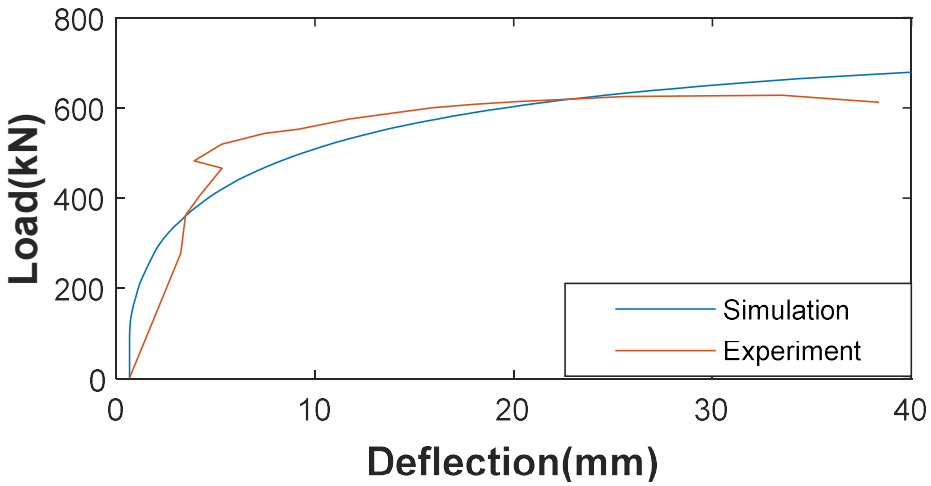

Figure 35. The comparison between big-scale laboratory tests and field test data.

## 5.3 Field Test Result

The testing results with all displacement sensors in the field test are shown in Figure 36 and Figure 37. The truck with a moving speed of ten mph, as shown in Figure 36. T6, and the truck with a moving speed of 40mph, as shown in **Error! Reference source not found.**7. In both figures, the LVDT(blue dash line) shows the highest displacement compared with the low-cost linear potentiometer (red line). The LVDT result has a clear waveform, while the linear potentiometer keeps ringing after the vehicle passed. That is because there is no damping or spring system in the linear potentiometer, while there is a spring in the LVDT device to make it not affected a lot from the vibration after the vehicle passes.

Comparing two results, the time duration of displacement of truck ten mph case(Figure 36. T6) is longer than truck 40mph case(**Error! Reference source not found.**7) because lower speed case needs more time to pass the bridge, which caused bridge response. The displacement amplitude are similar in both figures because both cases are use truck to test; the maximum displacement of LVDT is 0.1mm, and the low-cost linear potentiometer position sensor is0.07mm.

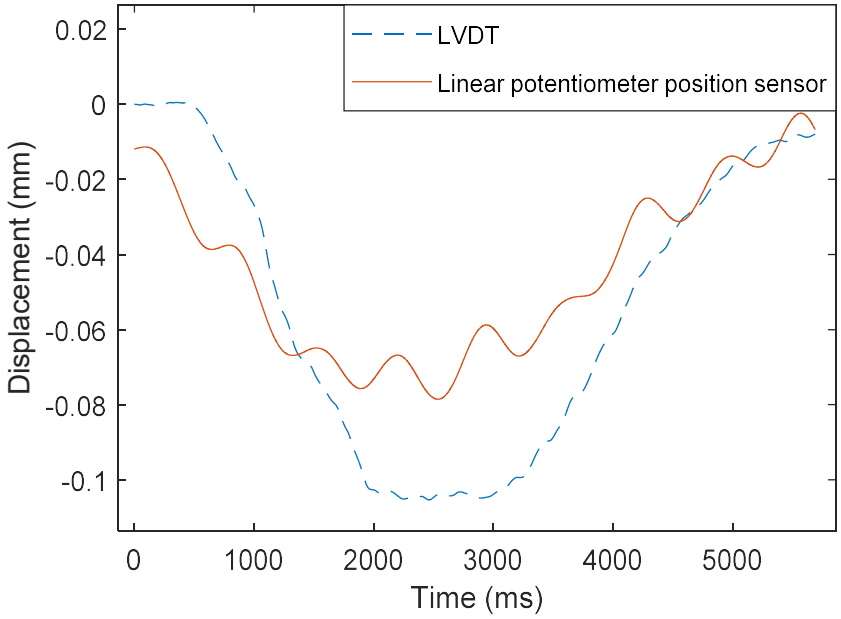


Figure 36. The displacement from field test (with truck 10mph)

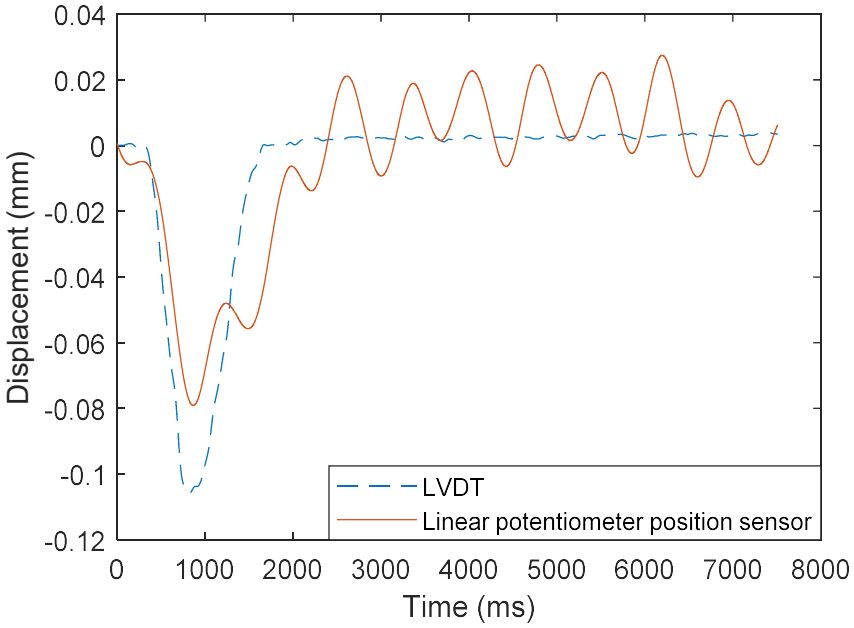


Figure 37. The displacement from field test (with truck 40mph)

The tendency curve between vehicle weight and moving speed is shown in Figure 38. The relationship between time of displacement variation and speed is presented in Figure 38(a). For all vehicles, when the speed is 10 mph has more time variation, while 40 mph has a shorter time. Thus, lower speed has more time to pass through the bridge. The statistical box plot with four vehicle cases presents in Figure 38(b), which is composed of the average and standard deviation. This box plot provides clear results only 10 mph case has more time difference between the four-vehicle test, the other two speed(25 and 40mph) has really close time variation between four different vehicle test.

The relations between maximum displacement peak and vehicle weight are in Figure 39 to Figure 41. Three algorithms is considered to find the relation between weight and displacement variation. The first one is calculated by maximum displacement (Figure 39), the second one is calculated by the total area of displacement variation (Figure 40), the last is calculated from the root mean square of the total area of displacement variation (Figure 41). All three algorithms show that the heavier weight causes a higher displacement value—the tendency curve between acceleration and different vehicles, as shown in Figure **42**. The acceleration is higher when speed is higher; the vehicle weight also affects acceleration which the heavier vehicle has higher acceleration—two examples of comparison between field test and simulation data as shown in Figure **43**. The case of a sedan with a 25 mph moving speed has a maximum displacement of 0.04 mm, while the van has a maximum displacement of 0.1mm. These two cases proved the developed FE simulation model with moving load(described in section 4.4.2) could simulate reality vehicle bridge interaction(VBI), demonstrating the reliability. Overall, for data analysis of field test, the weight affects displacement and acceleration; the moving speed also affects acceleration response.

For the future plan, these valuable field tests and proved simulation data can be used as input data for the machine learning(ML) model. Depending on the difference of displacement variance(or

other structural response), and vehicle weight, and moving speed, ML can provide the damage prediction information about bridge condition, and this information can be further used for structural health monitoring(SHM) evaluation.

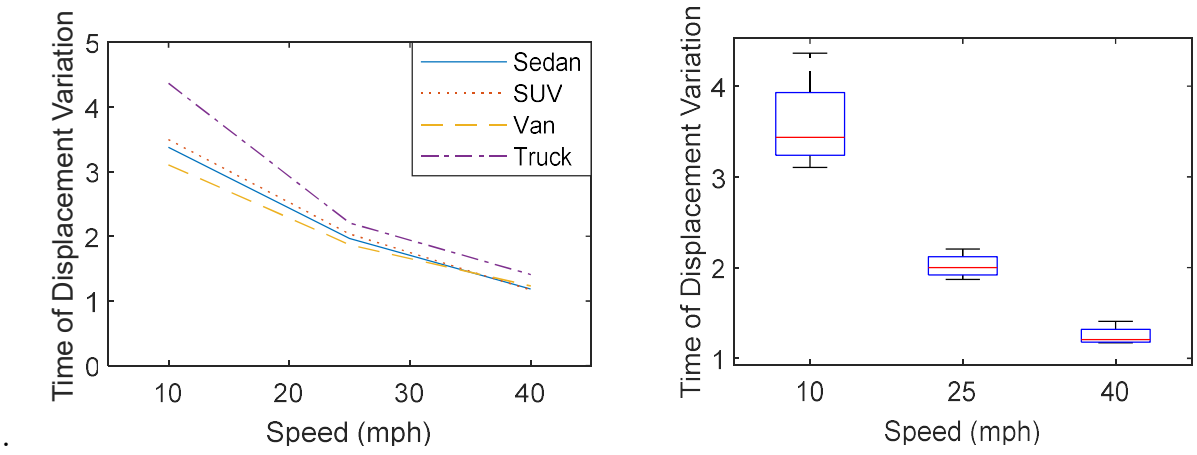


Figure 38. The tendency curve between speed and time of displacement variation when vehicles pass through the bridge. For all cases of vehicles, when the speed is 10 mph has more time variation, while 40 mph has a shorter time. Lower speed has more time to pass through the bridge causes this difference.

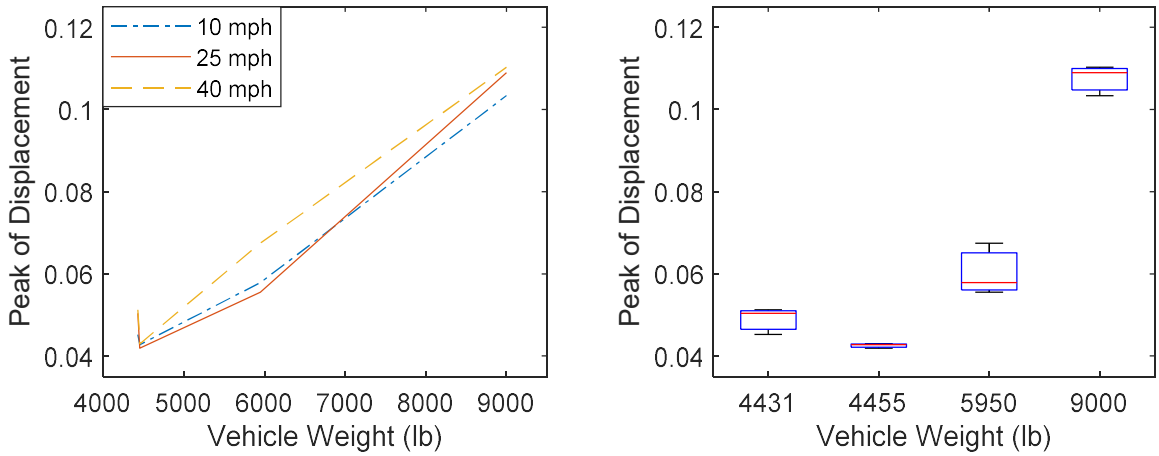


Figure 39. The tendency curve between vehicle weight and maximum displacement. Truck weight is 9000lb, van weight is 5950lb, sedan weight is 4431, and SUV is 4455 lb. Peak displacement is higher when the vehicle is heavier.

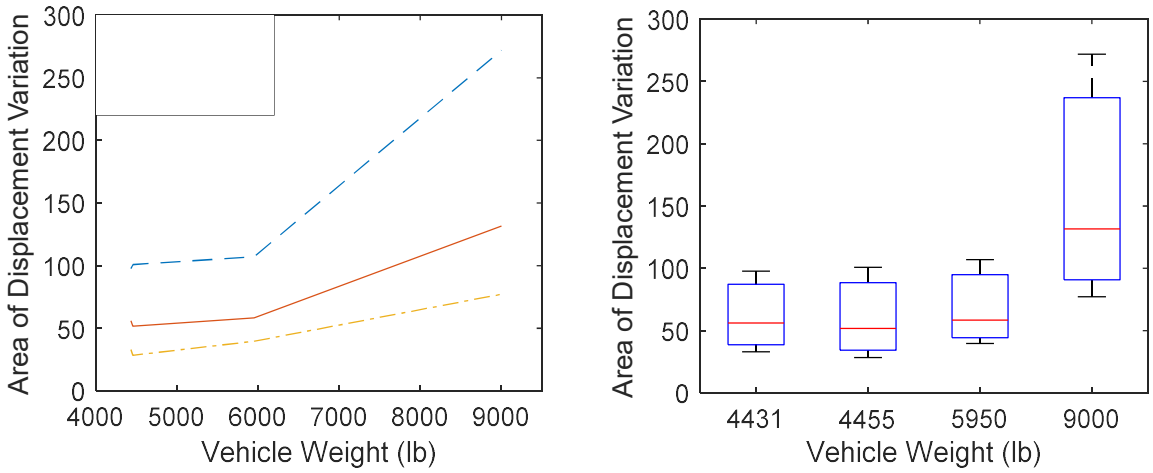


Figure 40. The tendency curve between vehicle weight and total area of displacement variation. Truck weight is 9000lb, van weight is 5950lb, sedan weight is 4431 and SUV is 4455 lb. The area of displacement variation is higher when the vehicle is heavier.

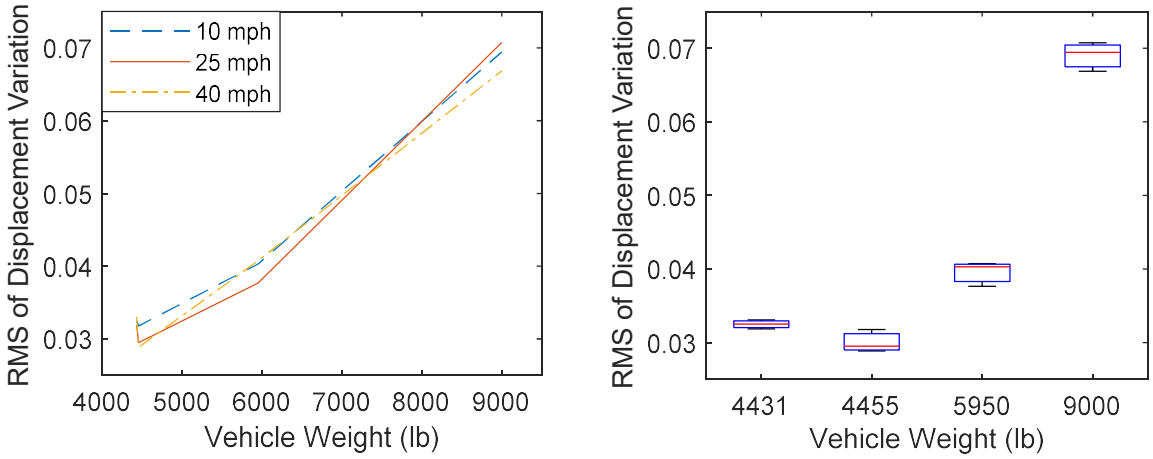


Figure 41. The tendency curve between vehicle weight and root mean square(RMS) of total area displacement variation. Truck weight is 9000lb, van weight is 5950lb, sedan weight is 4431 and SUV is 4455 lb. RMS of Area displacement variation is higher when a vehicle is heavier.

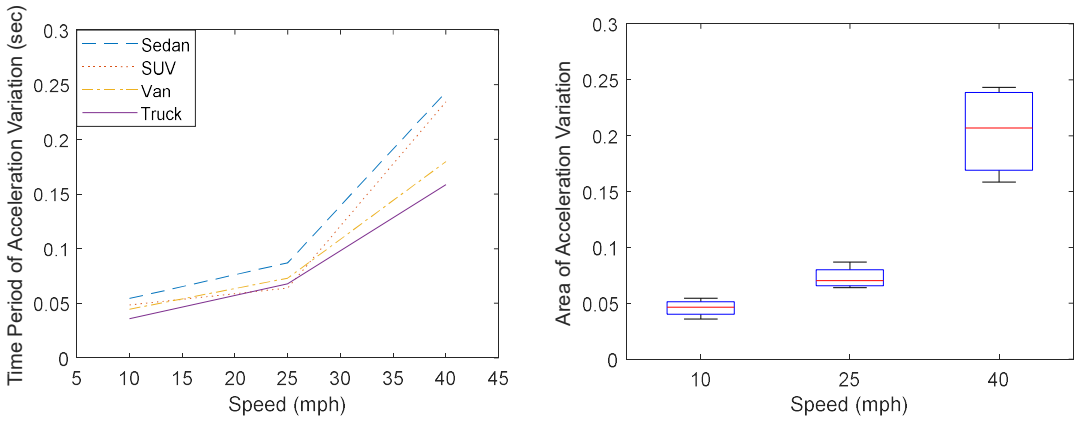


Figure 42. The tendency curve between acceleration and different vehicles. The acceleration is higher when speed is higher; the vehicle weight also affects acceleration which the heavier vehicle has higher acceleration. Truck weight is 9000lb, van weight is 5950lb, sedan weight is 4431, and SUV is 4455 lb.

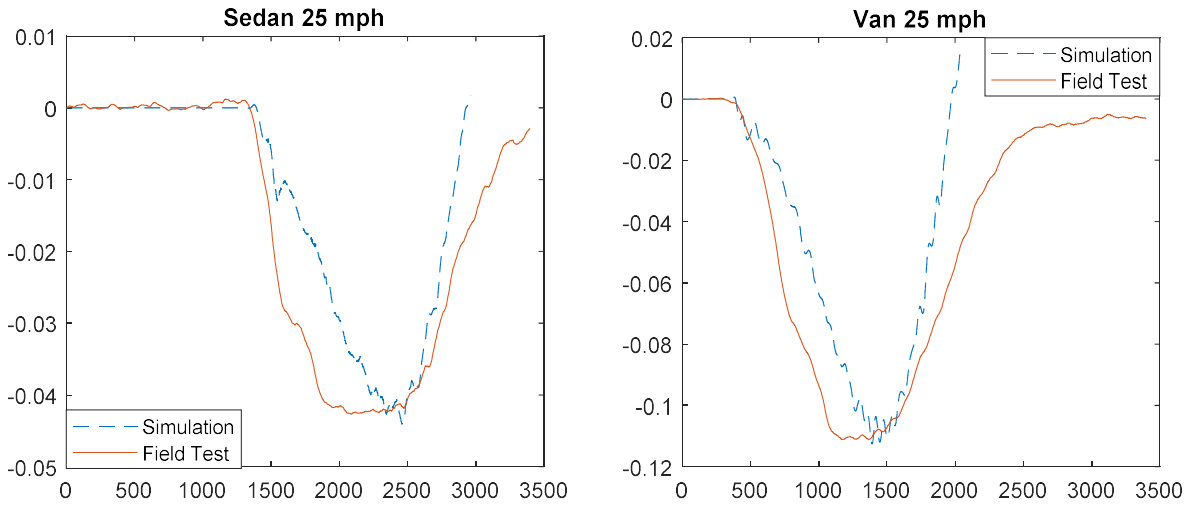


Figure 43. The comparison between field test data and simulation data. (a)Sedan 25mph case, and (b) Truck 25 mph case

## 5.4 In-depth Parameter Study of Finite Element Simulation Result

The bridge displacement of FE simulation applied with contact method for moving load with different parameters, which including 1) elastic modulus (E), 2) bridge density (D), 3) depth (H), 4) width(b), and 5) mesh size and the comparison results obtained from analytical solution **Error! Reference source not found.** are also shown in Figure 44 and Figure 45. The comparison of elastic modulus results between simulation and analytical solution is shown in Figure 44. The results show that the changing of elastic modulus did not bring the dramatic change of displacement because the bridge frequency is $= \frac{\pi^2}{L^2}\sqrt{\frac{EI}{m}}$, and the square root decreased the effect of elastic modulus. Besides, the amplitude of FE simulation and analytical results are not the same because the stiffness in the FE modeling could not give the exact same value as the analytical

solution. The stiffness between contact methods is automatically calculated by using the Lagrangian method discussed in section 4.4.2. The loss (%) of maximum displacement is shown in Figure 45, which shows the similar value between all cases that demonstrates FE simulation from the contact method, and the analytical solution has similar patterns for moving vehicle.

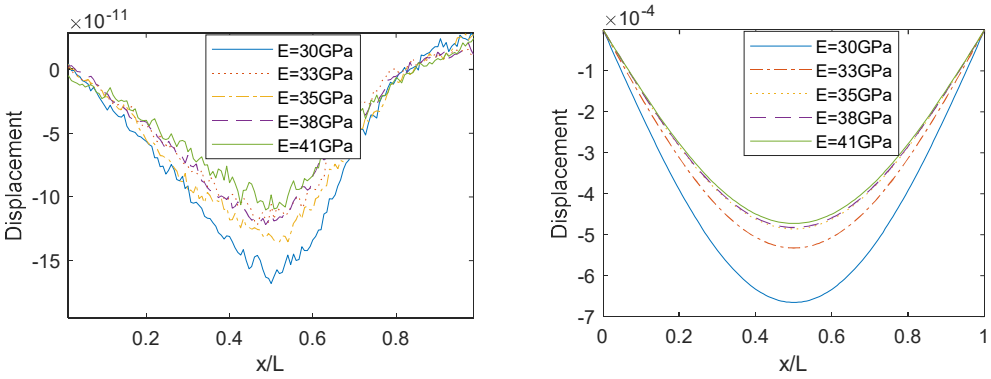


(a) FE simulation (b) Analytical solution

Figure 44. The bridge displacement of FE simulation(a) and analytical solution(b).

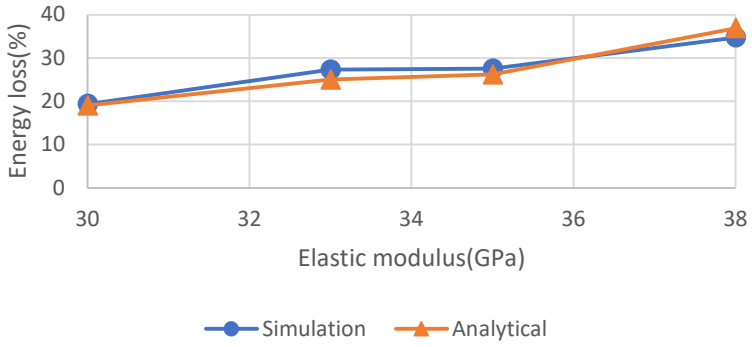


Figure 45. The loss (%) of maximum displacement. The value between FE simulation and analytical solution demonstrates similar energy loss, which means the FE simulation from contact method and analytical solution has similar pattern between for moving vehicle

The comparison density (D) results between simulation and analytical solution are shown in Figure 46. The results show a similar trend when D = 100 $\frac{kg}{m^3}$, which presents the negative maximum displacement of different density cases. Both results show that the lower density case has a higher displacement amplitude. Moreover, in the simulation results, the displacement does not start from 0 when bridge density is 100 $\frac{kg}{m^3}$ because the moving element density is 700$\frac{kg}{m^3}$ , which is higher than the bridge density. This may cause the phenomena where deformation occurs in the beginning. The individual comparison results of D=1000 $\frac{kg}{m^3}$ and 2400 $\frac{kg}{m^3}$ are shown in Figure 47. The waveform between simulation and analytical solution is similar in both cases. The shape is slightly different since the mass affects bridge frequency, and some high-frequency noise from reflected waves causes the zigzag shape in simulation results. To further prove the correctness of FE modeling, the loss (%) of maximum displacement between different density results is shown

in Figure 48. The percentage of energy loss between simulation and analytical solution shows a similar value, demonstrating the accuracy of FE simulation results. Note that stiffness is the only challenge parameter in the contact method of FE simulation. Since the stiffness is calculated automatically, it could not give the exact same value with analytical solation because it may cause a slight difference between results.

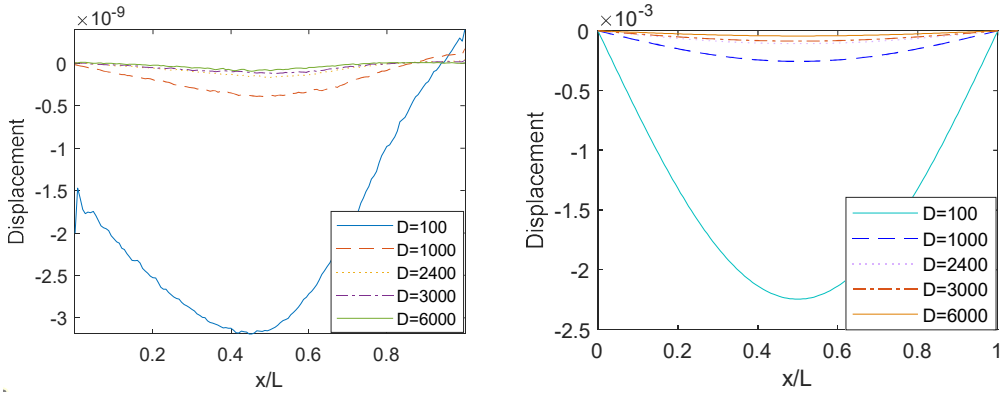


(a) FE simulation (b) Analytical solution

Figure 46. The comparison density results between simulation and analytical solution. They show a similar trend between different density cases, lower the density, higher the displacement. When D=100 in the simulation results, the displacement does not start from 0 because the moving element density (700 $\frac{kg}{m^3}$ ) is higher than bridge density (100 $\frac{kg}{m^3}$ ).

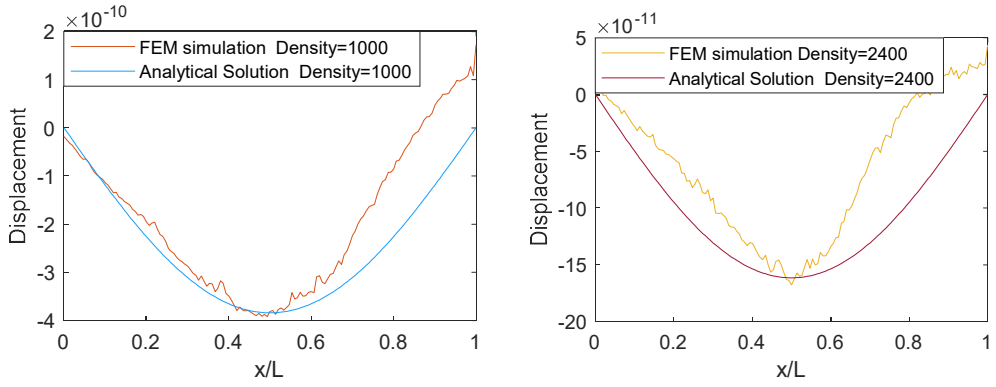


(a) Density=1000 (b) Density=2400

Figure 47. The individual results when density = 1000 and 2400. The simulation results demonstrate a similar shape with analytical solutions. However, the waveforms are slightly different because they are affected by high frequency reflected waves and the changing of bridge frequency.

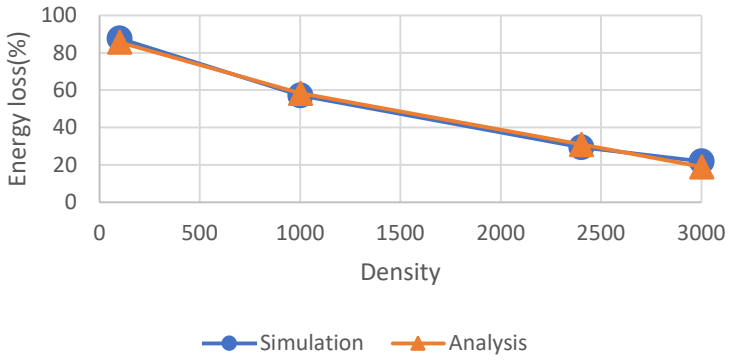


Figure 48. The loss (%) of maximum displacement between different density cases is based on Figure 47. The energy loss shows a similar decreasing percentage value between different density models and demonstrates the accuracy of FE simulation results. Note that the stiffness is the only challenge parameter in the contact method of FE simulation because the stiffness is calculated automatically and could not give the exact same value as the analytical solution, which may cause a slight difference between results.

The comparison of depth results is shown in Figure 49. The results show the trend in which the thinner depth model has a higher displacement amplitude. However, the waveform is highly affected by high-frequency reflected waves from the bottom sides, as shown in Figure 50. Depth = 0.1m shows the most fitting curve with the analytical solution; on the other hand, the depth = 0.5m shows shifting to the left with more high-frequency noise due to the depth difference and number of layers. More layers may cause more reflected waves, for example, the depth = 0.1 m case only has one layer in 0.1 m mesh size, but there are five layers in depth = 0.5m. The energy loss (%) of maximum displacement between different depth results is shown in Figure 51. The results show similar trends in which the energy loss keeps decreasing when depth is increasing. Therefore, the final moving load model is designed as 0.1m depth to minimize the effect of high-resolution noise.

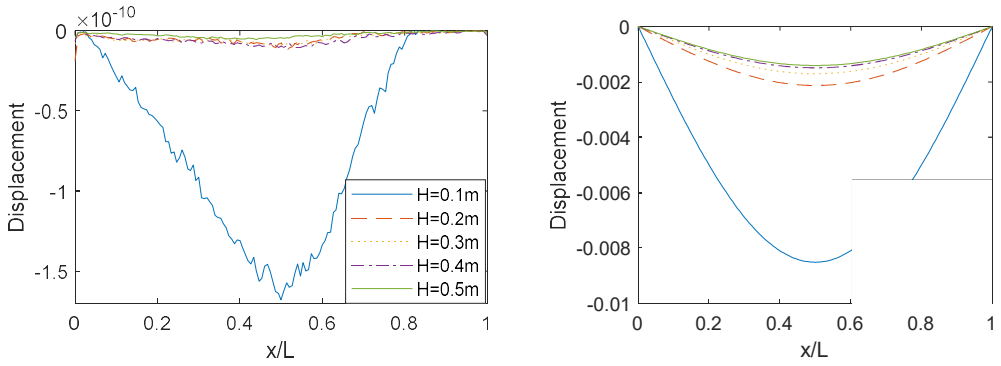


(a) FE simulation (b) Analytical solution

Figure 49. The comparison depth results between simulation and analytical solution. The results show the trend where the lower depth has higher displacement. However, the waveform is highly affected by high frequency reflected waves from bottom sides caused by thicker dimensions.

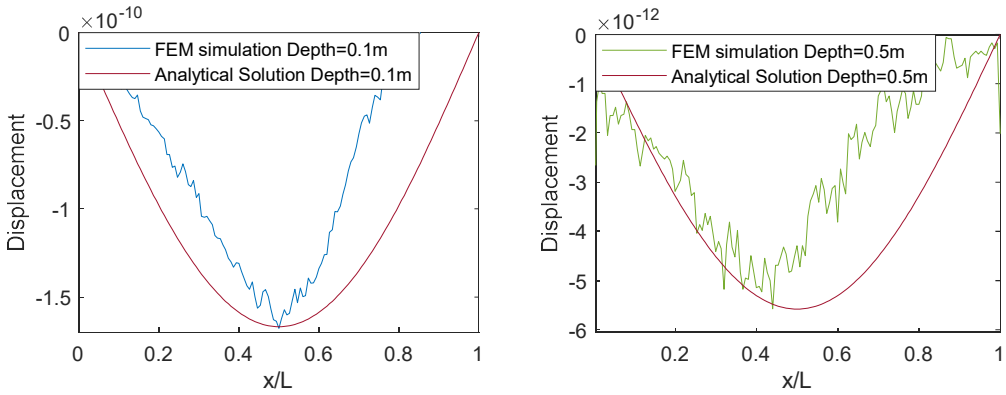


(a) Depth=0.3 m (b) Depth=2.5m

Figure 50. The individual results when depth = 0.1 m and 0.5 m. The 0.1m case shows a good fitting curve compared with the 0.5 m case due to the depth difference and number of layers. The deeper depth causes higher frequency noise. For instance, the depth =0.1 m case only has one layer, but there are five layers in depth = 0.5m case, which causes more reflected high-frequency noise.

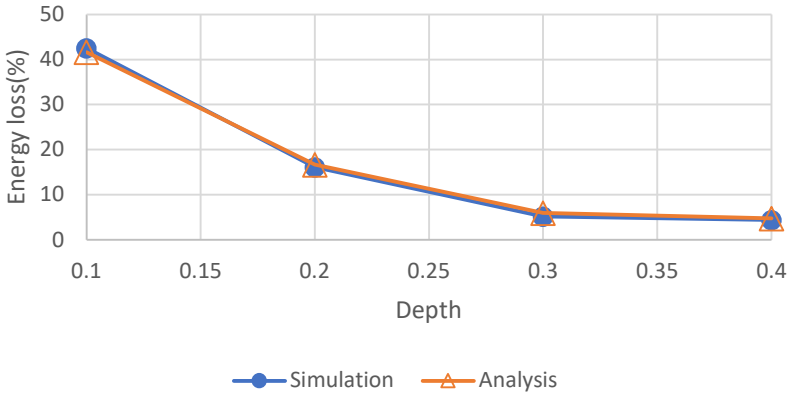


Figure 51. The loss (%) of maximum displacement between different depth cases is based on Figure 50. The energy loss shows a similar decreasing percentage value between different depth models. The results also show similar trends in which the energy loss keeps decreasing when depth is increasing.

The comparison of width results is shown in Figure 52. The reflected high frequency generated from the two-sided edge affects the waveform slightly. The larger width model has lesser high-frequency noise. The individual results of b=0.3 and b=2.5 are shown in Figure 53. In the b=0.3m case, the high-frequency noise affects waveform dramatically; however, in the case of width=2.5m, the effect from high-frequency noise is minor. The loss (%) of maximum displacement between different width (b) results are shown in Figure 54. Like other parameter studies, the energy loss shows similar trends between all FE simulations and analytical solutions.

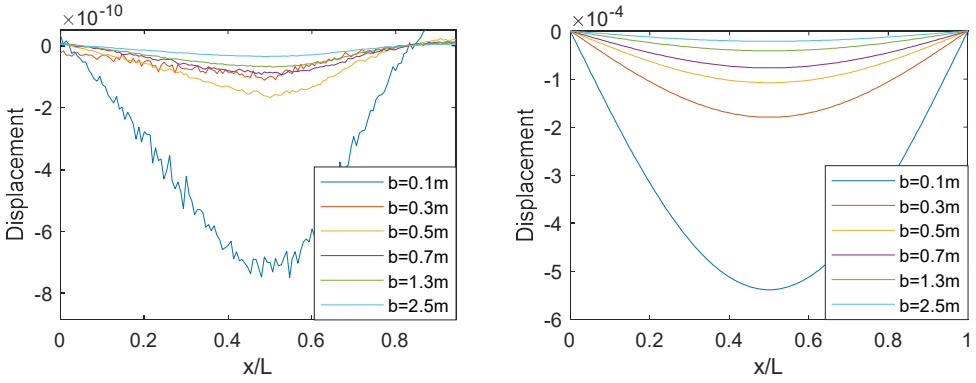


(a) FE simulation (b) Analytical solution

Figure 52. The comparison width results between simulation and analytical solution. The waveform for each case shows similar trends between simulation and analytical solutions. However, the smaller width causes more high-frequency noises.

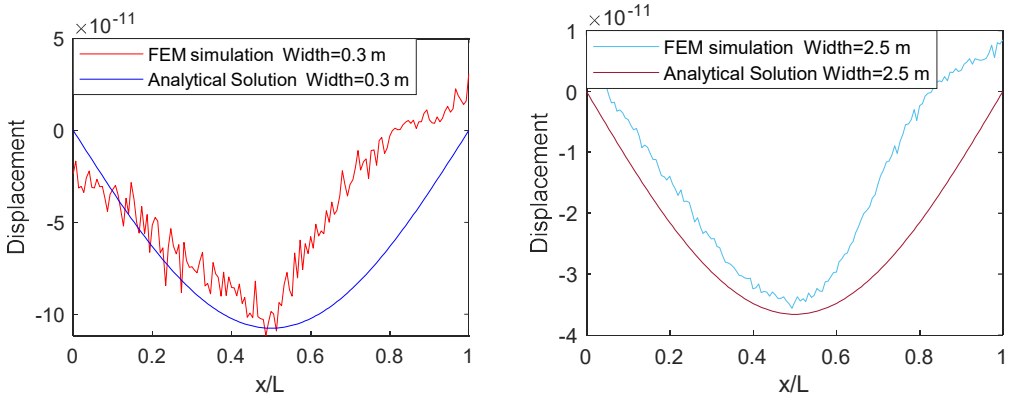


(a) Width = 0.3m (b) Width = 2.5m

Figure 53. The individual results when width = 0.1 m and 2.5 m. The case of width = 0.1m is affected by reflected high-frequency noise by two-side edges, but in the case of width = 2.5m, the reflected high-frequency noise affects waveform slightly.

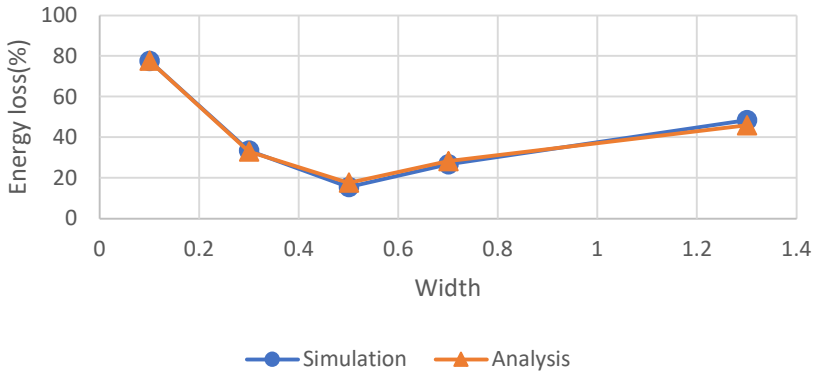


Figure 54. The loss (%) of maximum displacement between different width cases is based on Figure 53. The energy loss shows a similar decreasing percentage value between different width models

The comparison of mesh size results is shown in Figure **55**. According to Figure **55**(a), the amplitude is affected by mesh dramatically, and the smaller mesh size case (e.g., 0.025 m) has lower amplitude displacement. This is because the smaller mesh elements bring more interactions, such as reflections, between each element. Besides, in a smaller mesh case (0.025m), the interaction between elements affects the delay of signal, causing the shifting of the peak from $\frac{x}{L}$ =0.5 to 0.45 and obtains more high-frequency noise. Compared with 0.1 m and 0.05 m cases, more noise is obtained from 0.025 m cases because the smaller mesh size can obtain more high-resolution signals, including noise. The final model mesh size is 0.1m× 0.1 m to avoid high-resolution noise from the smaller mesh.

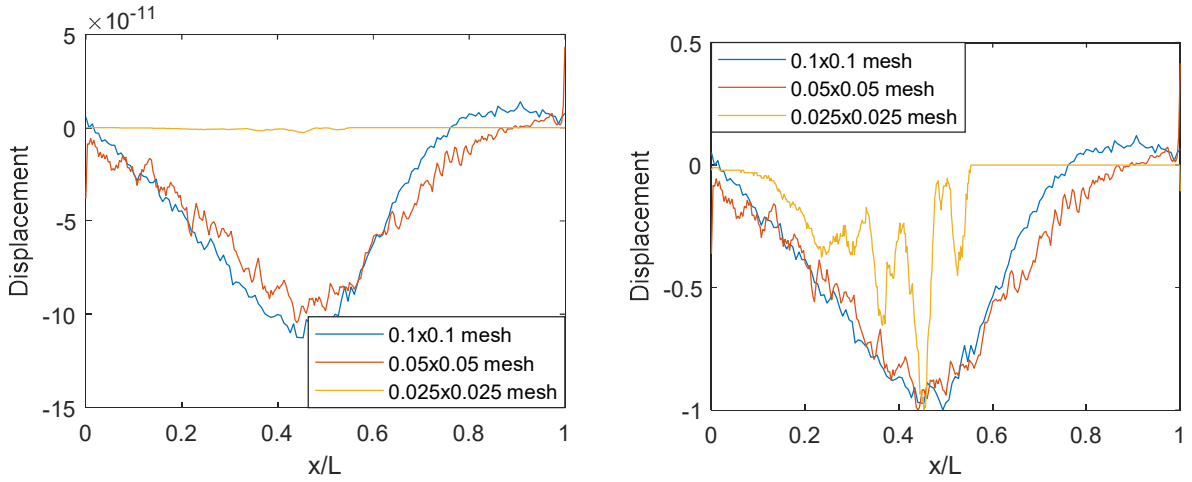


(a)FE simulation (original data) (b) FE simulation (normalized data)

Figure 55. The comparison mesh size results of the simulation. Compared with 0.1m and 0.05m mesh, the 0.025m mesh obtains more unnecessary high-frequency noise since the smaller mesh can gain a higher frequency signal, and its minimum peak is shifting from mid-span ( $\frac{x}{L} = \mathbf{0.5}$ to 0.45) because the signal is affected by the increasing element number.

## 5.5 Data Selection Result

The structural response of acceleration and its frequency generated with moving load applied with contact method with crack location 1 (CL1) case obtained from listening point (L8) is shown in Figure 56. The acceleration signal shows complicated patterns since the vehicle keeps sending the impulse on the bridge. It is impossible for human beings to classify the signal by different cracks, although finding the first four bridge frequencies in Figure 56 (b) is clear. Thus, ML is helpful to find the pattern between different crack cases. For example, the structural response (e.g., acceleration, displacement. and stress) and its statistical indicator are used as input to train the damage prediction model.

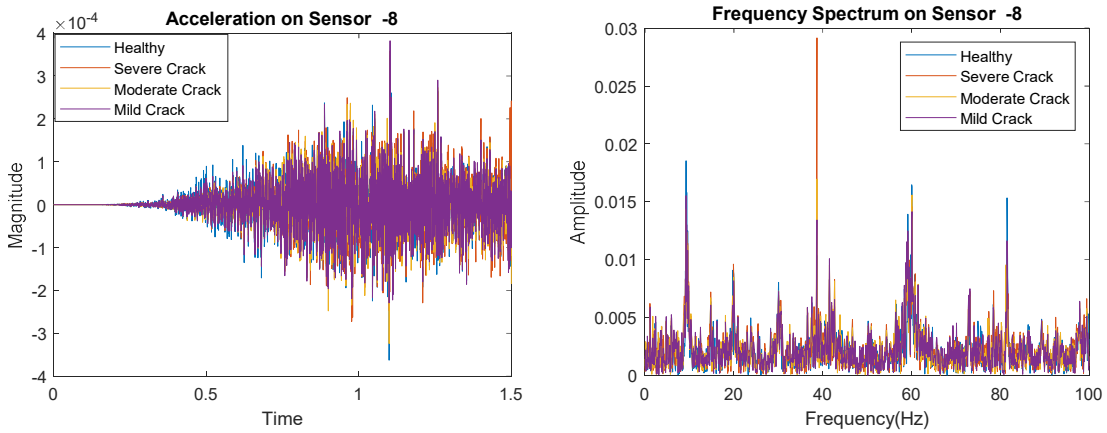


(a) Acceleration (b) Acceleration in frequency domain

Figure 56. One of the examples of structural responses of acceleration, frequency from FE simulation obtained from listening point (L8) with moving load model are shown in (a), (b), respectively. The structural responses from L1~L30 and its statistical indicator are used as input for the training damage prediction model.

Feature selection is used for ranking the importance of input data, which is used to improve the accuracy of the damage prediction model and decrease the computing time. The structural response (e.g., displacement, stress, acceleration, and acceleration in frequency domain) obtained from FE simulation used for input to calculate statistical indicator is shown in Table 8. The ranking importance based on Gini impurity is shown in Figure 57. The mean of acceleration has the highest importance regarding predicted results for damage prediction. Based on the Gini importance shown in $x$ axis, features with Gini important over 0.3 are used for training ML model for damage prediction.

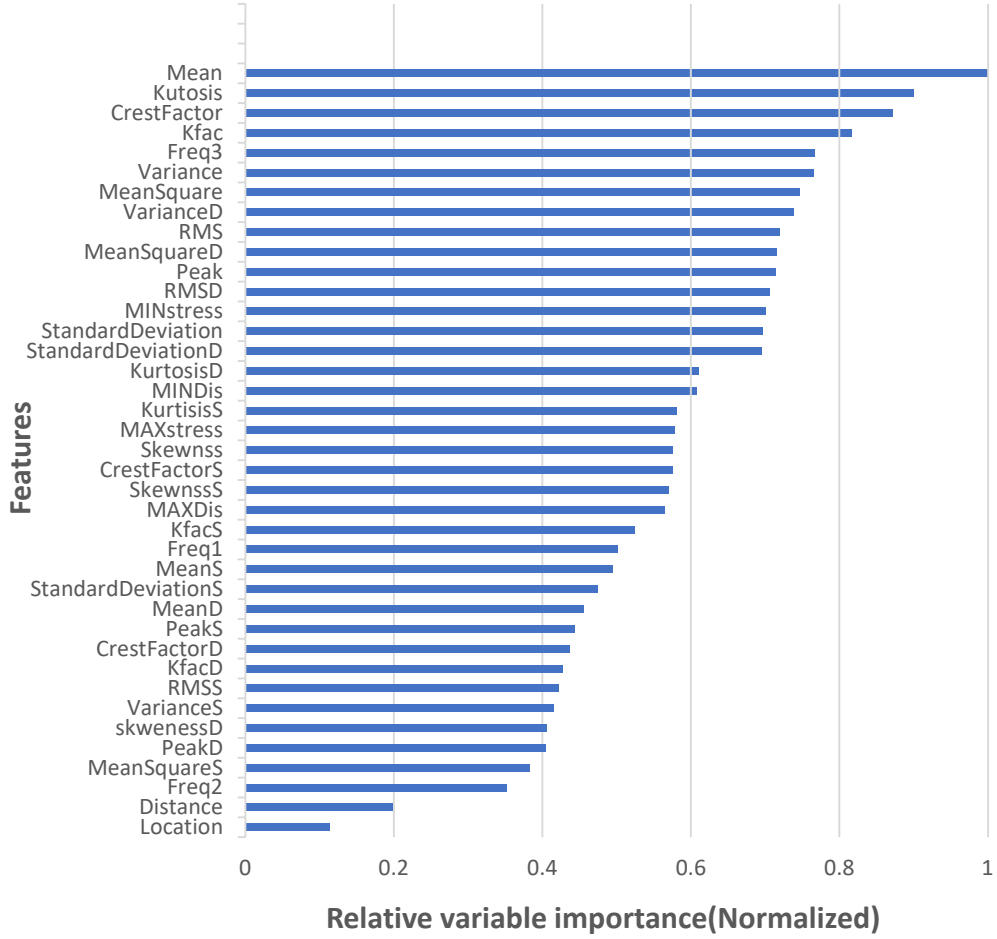


Figure 57. The importance ranking is calculated from the random forest with Gini impurity. The acceleration provides the highest importance feature for ML perdition results. The features with Gini importance over 0.3 are used in ML training data for damage prediction.

## 5.6 Damage Prediction Result

This section discusses the damage prediction of four classes of static load and moving load FE model using four different ML models, respectively. Although the static load is simple and easier to understand, the moving load condition is closer to realistic situations. The damage prediction results by using static load simulation results are shown in Figure 58. There are four classes of damage severity: 1) healthy, 2) mild crack, 3) moderate crack, and 4) severe crack based on the design of the FE model. The predicted results are called matching matrix, the real class is known information from FE model design, and the predicted class is the output from the ML model. The diagonal line shows the accuracy of damage prediction. The accuracy for prediction means the predicted class is matching with real class; for example, according to Figure 58(a), the accuracy of heathy, mild crack, moderate cracks, and the severe crack between real class and predicted class is 27.7%, 14.4%, 22.6%, and 25.6% separately. The total accuracy is the sum of these four values, showing an accuracy of 90.3%. For the static load model, XGBoost has the highest accuracy

(92.6%) to predict cracks. The second is BP, which shows 90.3% accuracy. SVM and DT have lower prediction results, which is expected because these two methods are based on statistical regression and classification methods. Once the input data is very complex (for example, structural response), the classification accuracy will be low, which means that the prediction model has not been well trained.

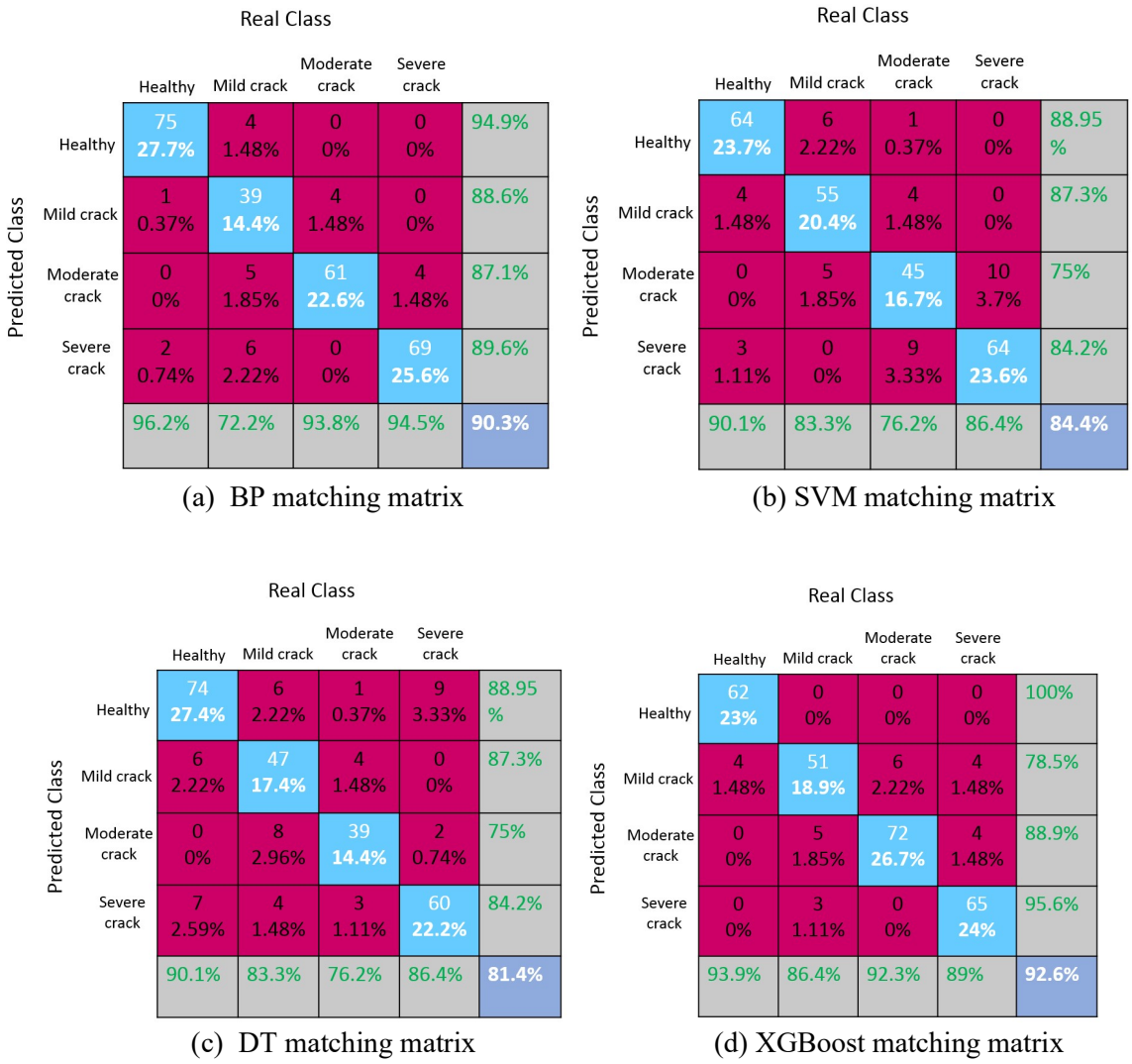


Figure 58. The damage prediction results by using static load FE simulation result. (a) BP, (b) SVM, (c) decision tree and (d) XGBoost. There are four classes of damage severity: 1) healthy, 2) mild crack, 3) moderate crack, and 4) severe crack based on the design of the FE model. The diagonal line shows the accuracy of damage prediction; for example, according to (a), the accuracy of heathy, mild crack, moderate crack, and the severe crack between real class and predicted class is 27.7%, 14.4%, 22.6%, and 25.6% separately. The summation of these four values displays 90.3% accuracy of the prediction model.

The prediction results applied with the contact method moving load are shown in Figure **59**. XGBoost has the highest prediction accuracy (83.3%), and the following are BP, DT, and SVM, with an accuracy of 80.5%, 77.9%, and 76.3%, respectively. Compared with the static load prediction model, the moving load prediction model shows lower accuracy for damage prediction since the structural response signal, known as input for the ML model, is much more complicated

than static load. For example, the impulse signal in the moving load model is always affected by continuous reflection generated from moving vehicles, and the bridge response is affected by complex impulse signals. Thus, the damage prediction accuracy in the moving load model is lower than the static load model, as expected. The prediction accuracy of each model is summarized in Table 10. The prediction accuracy of each model with two different load conditions. The XGBoost has the best damage prediction ability for four different crack cases.

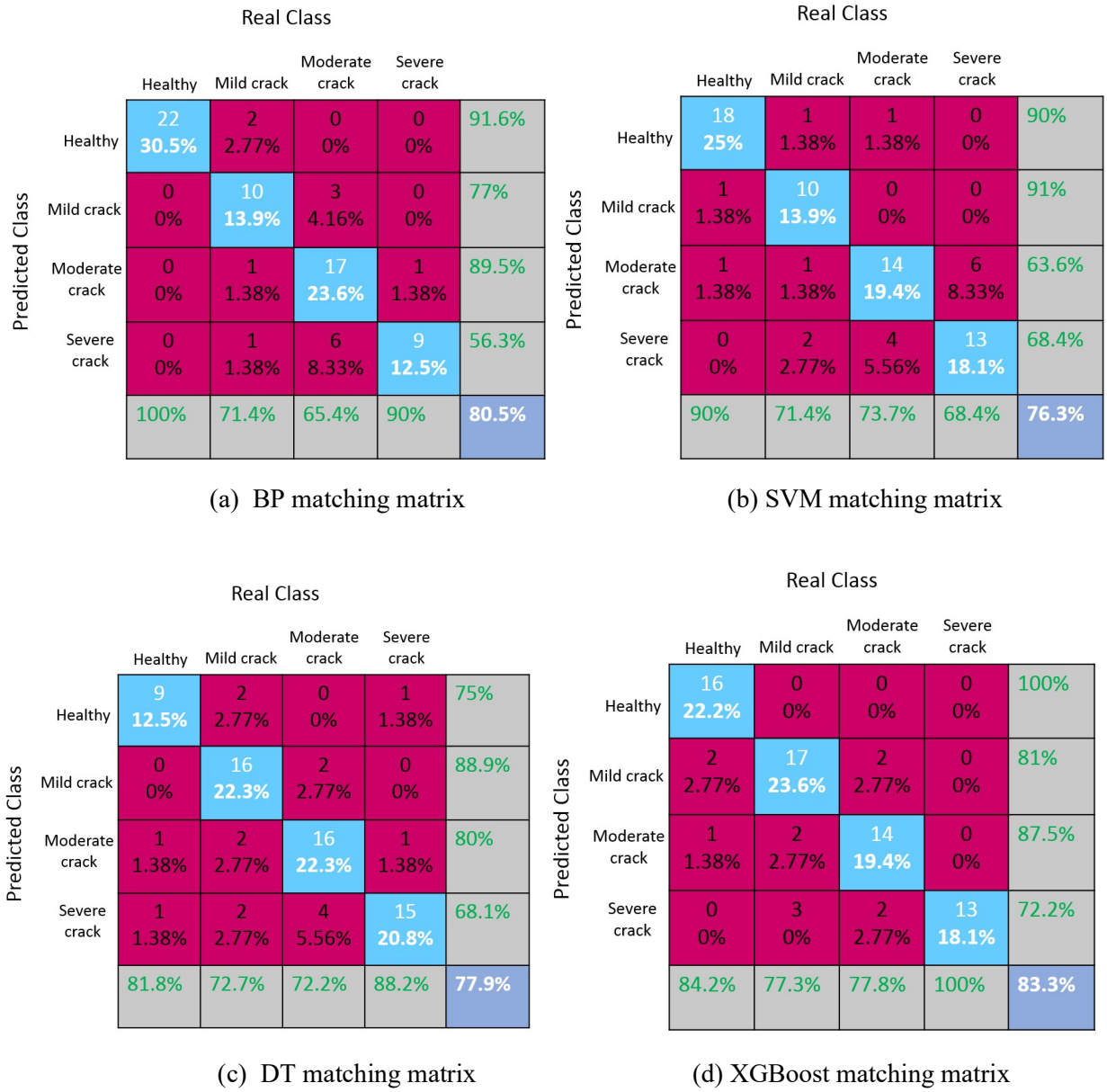


Figure 59. The damage prediction results by using moving load FE simulation result. (a) BP, (b) SVM, (c) decision tree and (d) XGBoost. There are four classes of damage severity: 1) healthy, 2) mild crack, 3) moderate crack, and 4) severe crack based on the design of the FE model. The diagonal line shows the accuracy of damage prediction; for example, according to (a), the accuracy of heathy, mild crack, moderate crack, and the severe crack between real class and predicted class is 30.5%, 13.9%, 23.6%, and 22.5% separately. The summation of these four values displays 80.5% accuracy of the prediction model.

Table 10. The prediction accuracy of each model with two different load conditions

| | BP | SVM | DT | XGBoost |
|---|---|---|---|---|
| Static load | 90.3% | 84.4% | 81.4% | 92.6% |
| Moving load | 80.5% | 76.3% | 77.9% | 83.3% |

# 6. CONCLUSIONS

In this study, the field test demonstrates low-cost sensor provides accurate data. The tendency curve explained the relation that includes vehicle weight, moving speed, and structural response. Furthermore, the developed contact method used for moving load FE simulation provides reliable and compatible data with real field test data. We developed a moving load FE model to simulate vehicle motion with contact method and finished the comprehensive parameter study of the FE model, which verified with VBI analytical solutions, and comparatively studied ML methods for damage prediction. Compared with the static load prediction model, the moving load prediction model shows lower accuracy for damage prediction since the structural response signal, known as input for ML model, is much more complicated than static load and much closer to real signals. Among four different ML models, XGBoost brings the highest damage prediction accuracy, with 92.6% accuracy for the static load model and 83.3% accuracy for the moving load model. The result demonstrates the new hope of damage prediction by using BWIM responses. In the future, once we build a bigger database with a structural response and consider many different healthy condition bridges, the ML approach developed in the project can be further improved and applied. The key findings are summarized below.

- First, the low-cost sensor is studied and applied as laboratory test with calibration and used in field tests. The low-cost sensor provides the other commercial option for vehicle bridge interaction(VBI) application.

- Second, the field test data further summarize to tendency curve between weight, speed, and structural response. The weight affects maximum displacement and acceleration, and speed affects acceleration.

- Third, the contact method used to simulate moving load is feasible, which the structural responses are verified with field test data and VBI analytical solution with comprehensive parameter studies. The loss (%) of maximum displacement between FE simulation results and VBI analytical solution shows a similar value.

- Fourth, feature selection is required for ML to avoid overfitting and minimize the situation where the ML prediction model is not well trained to increase the accuracy of damage prediction.

- Fifth, the prediction accuracy of moving load is lower than static load accuracy because the structural response with moving load is much more complicated than the response in static load model

- Last, by comparing the most recently used ML methods, XGBoost combines assembly decision tree and gradient boosting technology, allowing us to predict damage with the highest accuracy.

The series of procedures presented in this report has been performed with several different sensors, including low-cost sensors. The relation between different types of vehicles, weight, and size are tested. The collected field test data are compared with a simulation developed from the contact method. Furthermore, the ML model estimates and predicts structural damage from BWIM

signals, which brings a new strategy for cost-effective SHM. Such information will help structural engineers take preventive or proactive actions to improve the drivers' safety and protect and preserve the transportation infrastructure. Further research of the contact method concept with moving load will be further verified through the actual bridge field test to compare with real structural responses. The framework allows monitoring the health condition of the structure in real-time by using BWIM responses. For future work and plan, 1) the field test data with different healthy condition bridges should be collected which used to train the ML damage prediction model, 2) the field test should be including more different vehicle weights and speed to study deeper structural response patterns.

# REFERENCE


[1] V. I. Kolev, "Bridge Weigh-in-Motion Long-term Traffic Monitoring in the State of Connecticut," 2015.

[2] D. Cantero, R. Karoumi, and A. González, "The Virtual Axle concept for detection of localised damage using Bridge Weigh-in-Motion data," *Eng. Struct.*, vol. 89, pp. 26–36, 2015, doi: 10.1016/j.engstruct.2015.02.001.

[3] S. Z. Wen, W. C. Xiong, L. P. Huang, Z. R. Wang, X. Bin Zhang, and Z. H. He, "Damage and recovery of fiber Bragg grating under radiation environment," *Chinese Phys. B*, vol. 27, no. 9, 2018, doi: 10.1088/1674-1056/27/9/090701.

[4] E. OBrien, M. A. Khan, D. P. McCrum, and A. Žnidarič, "Using statistical analysis of an acceleration-based bridgeweigh-in-motion system for damage detection," *Appl. Sci.*, vol. 10, no. 2, pp. 2015–2019, 2020, doi: 10.3390/app10020663.

[5] E-C227, "Advancing Highway Traffic Monitoring Through Strategic Research," 2017.

[6] I. Gonzalez and R. Karoumi, "BWIM aided damage detection in bridges using machine learning," *J. Civ. Struct. Heal. Monit.*, vol. 5, no. 5, pp. 715–725, 2015, doi: 10.1007/s13349-015-0137-4.

[7] J. R. Gaxiola-camacho, J. Quintana, G. Esteban, V. Becerra, and F. J. Carrion, "Structural Health Monitoring of Bridges in Mexico -Case Studies Structural Health Monitoring of Bridges in Mexico – Case Studies," no. August, pp. 1–9, 2019.

[8] D. Cantero and A. González, "Bridge Damage Detection Using Weigh-in-Motion Technology," *J. Bridg. Eng.*, vol. 20, no. 5, p. 04014078, 2015, doi: 10.1061/(asce)be.1943-5592.0000674.

[9] S. Alampalli, M. M. Ettouney, and A. K. Agrawal, "Structural health monitoring for bridge maintenance," *Bridg. Struct.*, vol. 1, no. 3, pp. 345–354, 2005, doi: 10.1080/15732480500252751.

[10] J. M. Ko and Y. Q. Ni, "Technology developments in structural health monitoring of large-scale bridges," *Eng. Struct.*, vol. 27, no. 12 SPEC. ISS., pp. 1715–1725, 2005, doi: 10.1016/j.engstruct.2005.02.021.

[11] T. Heldt and C. T. Leader, "Bridge Management – Using Structural Health Monitoring," no. Table 1, pp. 1–10, 2019.

[12] D. Cantero and R. Karoumi, "The virtual axle concept for Bridge Weigh-in-Motion systems," *ICWIM8 - 8th Conf. Weigh-in-Motion*, no. June, pp. 51–60, 2019.

[13] A. C. Neves, I. González, J. Leander, and R. Karoumi, "A new approach to damage detection in bridges using machine learning," *Lect. Notes Civ. Eng.*, vol. 5, no. October, pp. 73–84, 2018, doi: 10.1007/978-3-319-67443-8_5.

[14] P. Chun, T. Yamane, S. Izumi, and N. Kuramoto, "Development of a Machine Learning-Based Damage," 2020.

[15] E. K. Chalouhi, I. Gonzalez, C. Gentile, and R. Karoumi, "Damage detection in railway bridges using Machine Learning: Application to a historic structure," *Procedia Eng.*, vol. 199, pp. 1931–1936, 2017, doi: 10.1016/j.proeng.2017.09.287.

[16] A. Valadarsky, M. Schapira, D. Shahaf, and A. Tamar, "A machine learning approach to routing," *arXiv*, 2017.

[17] S. Gridnev and I. Ravodin, "Finite element modeling of a moving load using contact conditions," *MATEC Web Conf.*, vol. 196, pp. 1–8, 2018, doi: 10.1051/matecconf/201819601044.

[18] J. C. Simo and T. A. Laursen, "An augmented lagrangian treatment of contact problems involving friction," *Comput. Struct.*, vol. 42, no. 1, pp. 97–116, 1992, doi: 10.1016/0045-7949(92)90540-G.

[19] M. Hirmand, M. Vahab, and A. R. Khoei, "An augmented Lagrangian contact formulation for frictional discontinuities with the extended finite element method," *Finite Elem. Anal. Des.*, vol. 107, pp. 28–43, 2015, doi: 10.1016/j.finel.2015.08.003.

[20] M. Hirmand, M. Vahab, and A. R. Khoei, "An augmented Lagrangian contact formulation for frictional discontinuities with the extended finite element method," *Finite Elem. Anal. Des.*, vol. 107, pp. 28–43, 2015, doi: 10.1016/j.finel.2015.08.003.

[21] E. J. OBrien, A. Malekjafarian, and A. González, "Application of empirical mode decomposition to drive-by bridge damage detection," *Eur. J. Mech. A/Solids*, vol. 61, no. January 2019, pp. 151–163, 2017, doi: 10.1016/j.euromechsol.2016.09.009.

[22] Y. B. Yang, C. W. Lin, and J. D. Yau, "Extracting bridge frequencies from the dynamic response of a passing vehicle," *J. Sound Vib.*, vol. 272, no. 3–5, pp. 471–493, 2004, doi: 10.1016/S0022-460X(03)00378-X.

[23] R. P. Finotti, A. A. Cury, and F. de S. Barbosa, "An SHM approach using machine learning and statistical indicators extracted from raw dynamic measurements," *Lat. Am. J. Solids Struct.*, vol. 16, no. 2, pp. 1–17, 2019, doi: 10.1590/1679-78254942.

[24] B. Venkatesh and J. Anuradha, "A review of Feature Selection and its methods," *Cybern. Inf. Technol.*, vol. 19, no. 1, pp. 3–26, 2019, doi: 10.2478/CAIT-2019-0001.

[25] L. Deng and D. Yu, "Deep learning: Methods and applications," *Found. Trends Signal Process.*, vol. 7, no. 3–4, pp. 197–387, 2013, doi: 10.1561/2000000039.

[26] H. F. Chen, "In silico log p prediction for a large data set with support vector machines, radial basis neural networks and multiple linear regression," *Chem. Biol. Drug Des.*, vol. 74, no. 2, pp. 142–147, 2009, doi: 10.1111/j.1747-0285.2009.00840.x.

[27] J. Friedman, R. Tibshirani, and T. Hastie, "Additive logistic regression: a statistical view of boosting (With discussion and a rejoinder by the authors)," *Ann. Stat.*, vol. 28, no. 2, pp. 337–407, 2000, doi: 10.1214/aos/1016120463.

[28] T. Chen and C. Guestrin, "XGBoost: A Scalable Tree Boosting System," *Proc. 22nd ACM SIGKDD Int. Conf. Knowl. Discov. Data Min.*, pp. 785–794, 2016.